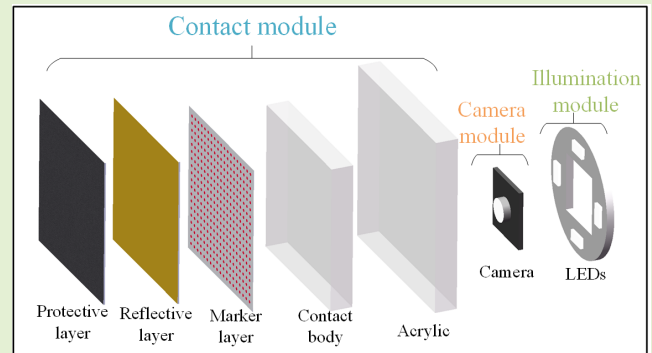


# Hardware Technology of Vision-Based Tactile Sensor: A Review

Shixin Zhang<sup>1</sup>, Zixi Chen<sup>1</sup>, Yuan Gao<sup>1</sup>, Weiwei Wan<sup>1</sup>, *Senior Member, IEEE*, Jianhua Shan,  
Hongxiang Xue, Fuchun Sun<sup>2</sup>, *Fellow, IEEE*, Yiyong Yang, and Bin Fang<sup>3</sup>, *Member, IEEE*

**Abstract**—A vision-based tactile sensor (VBTS) is an innovative optical sensor widely applied in robotic perception. The VBTS consists of a contact module, an illumination module, and a camera module. Its hardware technologies contain preparation, performance, functions, materials, and optimization design of components. However, the current literature lacks a review of hardware technologies to formulate a complete manufacturing scheme. Therefore, this article focuses on hardware technologies and reviewed the literature over the past five years. We analyze the core components of each module and sort out a technical route. The current challenges and problems of hardware technologies are discussed to propose some feasible solutions. Considering cross-disciplinary applications, we think that multidisciplinary hardware technologies are expected to promote the development of next-generation VBTSs. In addition, we aim to provide a valuable guideline for developers to improve the performance of VBTSs.

**Index Terms**—Camera module, contact module, illumination module, vision-based tactile sensor (VBTS).



## I. INTRODUCTION

VISION and touch are the most widely used perception modes in robot interaction. To simulate tactile mechanisms, researchers usually adopt electronic tactile sensors, such as resistive sensors, capacitive sensors, and fiber sen-

sors [1], [2], [3], [4]. However, these sensors have limitations in tactile feedback and high-resolution tactile information, which limits robotic perception and operation performance.

Since images contain a large amount of information that is easy for automatic processing, computer vision is widely used to replace the human eyes to measure and detect objects. Through the visual representation of tactile information, the vision-based tactile sensor (VBTS) can improve the quality of tactile information. Currently, the representative sensors include Gelsight [5], [6], and Tactip [7]. VBTSs have developed a variety of functions, such as texture recognition [8], multidimensional force detection [9], and temperature detection [10] as shown in Fig. 1(a) and (b). They were also applied to several fields, including robots, industrial detection, and human-computer interaction [see Fig. 1(d) and (e)]. For example, it can improve robotic ability of perception-manipulation, including posture recognition [11], [12] and flexible grasp [13] [see Fig. 1(c)]. VBTSs can solve the detection problem of fabric defects [14], and the texture and temperature of transparent objects [15] [see Fig. 1(f) and (g)].

Compared with electronic tactile sensors, VBTSs have six advantages as follows.

- 1) *High-Resolution Information*: Because images can provide continuous tactile information, visual representation alleviates the problem of sparse information.
- 2) *High Robustness*: VBTSs can reduce environmental interference, such as temperature and magnetic field interference, to enhance robustness.

Manuscript received 20 August 2022; revised 22 September 2022; accepted 22 September 2022. Date of publication 4 October 2022; date of current version 14 November 2022. This work was supported in part by the National Natural Science Foundation of China under Grant 62173197 and Grant 91848206, in part by the State Key Laboratory of Automotive Safety and Energy under Grant KF2006, and in part by the Natural Science Foundation of Anhui Province under Grant 2108085MF224. The associate editor coordinating the review of this article and approving it for publication was Prof. Carlos Marques. (Shixin Zhang, Zixi Chen, and Yuan Gao contributed equally to this work.) (Corresponding author: Bin Fang.)

Shixin Zhang and Yiyong Yang are with the School of Engineering and Technology, China University of Geosciences (Beijing), Beijing 100083, China (e-mail: zhangshixin@email.cugb.edu.cn; yangyy@cugb.edu.cn).

Zixi Chen, Fuchun Sun, and Bin Fang are with the State Key Laboratory of Intelligent Technology and Systems, Beijing National Research Center for Information Science and Technology, Department of Computer Science and Technology, Institute for Artificial Intelligence, Tsinghua University, Beijing 100084, China (e-mail: czx980730@gmail.com; fcsun@tsinghua.edu.cn; fangbin@tsinghua.edu.cn).

Yuan Gao and Weiwei Wan are with the Department of System Innovation, Graduate School of Engineering Science, Osaka University, Toyonaka, Osaka 560-8531, Japan (e-mail: hjczgaoyuan@gmail.com; wan@sys.es.osaka-u.ac.jp).

Jianhua Shan is with the Anhui Province Key Laboratory of Special Heavy Load Robot, Anhui University of Technology, Ma'anshan 243002, China (e-mail: 379751793@qq.com).

Hongxiang Xue is with the Institute of Engineering and Application, Fudan University, Shanghai 200433, China (e-mail: 21110860018@m.fudan.edu.cn).

Digital Object Identifier 10.1109/JSEN.2022.3210210

- 3) *Simplified Circuit*: VBTSs integrate electronic components and reduce wire arrangement.
- 4) *Low Cost*: The compact structure and inexpensive hardware of VBTSs decrease the manufacturing cost.
- 5) *Multimodality*: The multimodal functions of the camera boost the modal development and integration of VBTSs.
- 6) *Multimodal Fusion*: Since VBTS's data are presented in the form of images, it improves the fusion efficiency of visual and tactile information.

VBTSs extract tactile information from tactile images through image processing. For example, the contact point is identified by locating the deformation regions [16], [17]. The mapped shape [18], [19] or the fine texture [20], [21] is obtained by extracting the geometric features or contour of the deformation regions. By tracking the displacement of markers, the force distributions are detected and constructed [22], [23], such as the normal force [24], [25] and shear force [26], [27]. The applications of deep learning in image recognition also indirectly promote the development of VBTS, especially enhancing the multimodal perception performance. Yuan et al. [28] estimated the hardness of objects via a convolutional neural network (CNN) recognizing deformation degree, the change in brightness, and the displacement of markers. Based on the deformation degree and texture features, VBTSs provided the discrimination of fabric property [29] and comfort [30]. Li et al. [31] realized object shape recognition and 3-D reconstruction by learning geometric features of the deformation region by ConvNets. Jiang et al. [32] detected cracks on object surfaces by Deeplabv3 to capture deformation.

Owing to excellent perception and sensitive force feedback, VBTSs have been applied in operation tasks. By detecting marker displacement, Song et al. [33] adjusted the grasping force in the insertion operation, and Dong and Rodriguez [34] avoided cargo collision in the dense packaging task. By locating the contact regions and calibrating markers, the robot can formulate instance grasping [35], judge the success rate of grasping [36], and adjust the grasping strategy [37], [38], [39]. Through the angle feedback, the manipulator can control the swing angle to match the direction of stringing [40] or assembling [41]. In [42], the optical flow information of the markers provided rotation feedback to control the swing of each joint and predict the swing angle.

As described in [43], VBTSs have the potential to provide robots with better perception performance. In recent years, some reviews have introduced sensor types [44], [45], perception methods [46], and perception applications [47], including Yuan et al. and Alexander et al., who, respectively, reviewed Gelsight sensors in 2017 [48] and 2020 [49], and Lepora et al., who reported the related works of Tactip sensors in 2017 [50] and 2021 [51]. Abad and Ranasinghe [49] sorted out the development history of VBTSs to establish the research system of the visual-tactile mechanism. It is worth noting that size optimization and hardware improvement have promoted the miniaturization and multimodal development of VBTSs in recent years. In this review, we survey the hardware technologies of VBTSs over the past five years and highlight their importance. Referring to [44] and [49], it is necessary

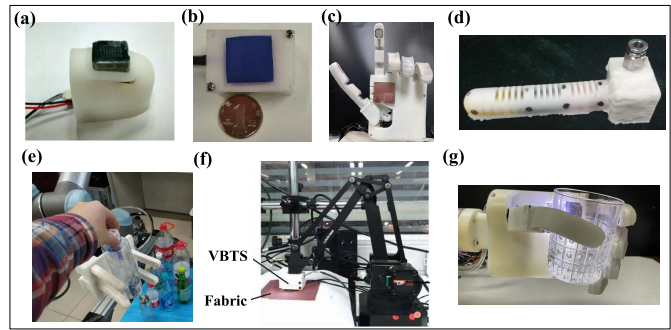


Fig. 1. TH-Tactile sensor and its operation applications. (a) It can detect contact force and texture [8]. (b) It developed a temperature perception modality [10]. (c) Multimodal VBTS was embedded into a variable-stiffness soft hand [13]. (d) It was applied to the soft hand to detect the bending direction and degree [12]. (e) Interaction with soft hand. (f) Detection of fabric defects [14]. (g) Detection of the texture of transparent objects [15].

to expand hardware analysis to the other VBTSs instead of limiting it to the representative VBTSs. Therefore, this article summarizes and analyzes the hardware technologies from hardware types, materials, preparation processes, performance, and integration technology. Compared with previous reviews, we only focus on hardware technology rather than specific sensor design. We hope that it will supplement the other reviews with hardware technologies and serve as a reference to the development of VBTSs.

## II. STRUCTURE AND PRINCIPLE OF VBTS

A VBTS is an innovative optical sensor. The main structure consists of a contact module, an illumination module, a camera module, and an information processing module. Because the information processing module is independent of the sensor, this article will not discuss it in detail. Fig. 2 shows the general structure of VBTSs and the sensing mechanism.

The contact module is the core of the entire sensor, which contains the contact body, the reflective layer, the protective layer, and the marker layer. The illumination is the basis of imaging, so the camera module and the illumination module are regarded as a whole. Vertical illumination is the simplest method to obtain stable and uniform illumination. With the modular development of LEDs, the optical path design is more refined, especially in limited space. Microcamera technology has a balanced size and imaging performance, indirectly promoting the development of micro-VBTSs.

VBTSs record and process images to obtain tactile information. When light emitted from the light source is reflected by the reflective layer and transmitted to the camera, the camera captures brightness differences to form tactile images. Some functional layers represent different perception mechanisms. We will introduce the sensing principle through the reflective layer and the marker layer.

When the reflective layer deforms along the contact surface, the deformation regions cause irregular shifts in the reflection path. This causes RGB differences in the tactile images, so the contact regions visually contrast with the surroundings [52], as shown in Fig. 2(b). Since the reflective layer has a high sensitivity to brightness, the tiny deformation can be presented significantly in the image.

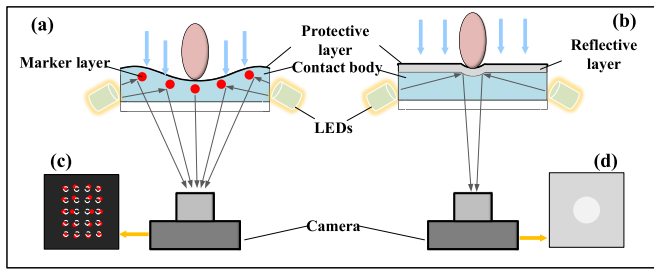


Fig. 2. Sensing principle of VBTS. (a) Markers move with the deformation of the contact body. Their displacement and direction represent the force magnitude and distribution. (b) Surface deformation causes irregular refraction of light. The brightness differences in the tactile images reflect contact regions. (c) and (d) Tactile images under two sensing principles.

The markers as a reference can relatively reflect and measure the deformation state of the contact body. As shown in Fig. 2(a), the marker array moves relative to the initial state under pressure [53]. The contact regions (namely, the stick-center region [54]) sink and spread out to the surrounding regions [55]. When the contact surface is twisted, the optical flow shows the rotation state [56].

### III. CONTACT MODULE

#### A. Contact Body

1) *Material*: The main forms of the contact body are elastomer and elastic skin. Silicone is a widely used material for preparing contact bodies because of its resilient property. Some researchers have also adopted latex materials [57], [58], [59] because elastic and inflatable latex films have better flexibility to fit the shape of the detected object [60]. In addition, the detection range of the inflated latex film is wider than that of silicone. However, latex cannot meet the requirements of high transparency and hardness. Most of the time, silicone is an optimal scheme. The position of markers is related to the transparency of the contact body. For example, the transparent contact body can present the external surface or internal deformation. In addition to transparent silicone, it includes translucent and colored silicone.

a) *Transparent/translucent silicone*: Gelsight sensors detected the deformation of the contact regions on the external surface. As a result, their series of sensors adopted the highly transparent and colorless silicone material XP-565 (Silicones, Inc.) as shown in Table I. Due to its reliable physical properties, other researchers have followed this scheme in their sensors, such as [61], [62], [63], and GelSlim [64]. Solaris is a highly transparent silicone from Smooth-On Company. Du et al. [65] used it to fabricate a high-performance contact body with 20-A hardness (the official reference hardness is 15 A). To achieve high sensitivity to deformation, the researcher adopted SilGel 612 silicone (low hardness and high transparency) produced by WACKER Company [8]. In [66], another WACKER silicone (ELASTOSIL RT 601 RTV-2) was used to prepare a transparent silicone layer with a medium-level hardness (45 A).

In addition to Solaris, Smooth-On offers translucent silicone with different hardnesses (see Table I). Soter et al. [67] used Sorta-Clear 12 silicone to prepare elastomer with 12-A hard-

ness. Kappassov et al. [68] adopted Sorta-Clear 18 silicone. The curing time was doubled that of Sorta-Clear 12, but the hardness was increased to 18 A. In [69], the curved silicone layer was made of highly elastic translucent silicone (Dragon Skin 20, Smooth-On, 20 A) that was close to the hardness of human skin. To prepare the softer contact body, Ecoflex 50 and Ecoflex GEL can achieve hardnesses of 00–50 and 000–35 A, respectively. For example, researchers used them to prepare elastic skin and a soft silicone layer [70], [71]. We think translucent silicone mainly provides high resilient deformation rather than imaging performance similar to transparent silicone.

b) *Colored silicone*: The colored silicone can increase image contrast and block out external light. Some silicone has a self-color (see Table I). For example, Ward-Cherrier et al. [50] used off-white and high-hardness silicone Vytaflex 30 and 60 (Smooth-On, Inc.) to fabricate the outer surface skin of the Tactip sensor. In [70], the tip was made of platinum-catalyzed EcoFlex 50, and the inner surface was coated with white paint. Polic et al. [72] selected black as the tip color to distinguish the background from the markers. Yu et al. [69] reported the dyeing process by adding black silicone dye to the silicone solution. Researchers should consider the effect of silicone color on contact bodies. For example, in [73], the activation temperature of SFXC thermochromic powder was 31°C, below which the powder was black, and above which the powder was white. The reason for choosing Vytaflex 30 was that the silicone color did not affect the color presentation of thermochromic powder at different temperatures. In [12], the tricolor elastic inner cavity was prepared by WACKER SilGel 612 and multicolored fluorescent powders [11]. Consequently, the transparent silicone enabled the color of the inner cavity to be consistent with the fluorescent powders.

c) *Mixture ratio*: Hardness is related to spatial resolution and sensitivity. The low hardness possibly achieves maximum sensitivity and resolution, but the soft characteristics cause two problems: low tensile strength and high viscosity.

Most types of silicone have a specific ratio and a fixed hardness, but there is some silicone with adjustable ratios, such as XP-565. The suitable hardness for Gelsight sensors is 5~20 A [48], so developers are constantly adjusting hardness to achieve an optimal perception effect. Romero et al. [74] proposed a fingertip sensor integrated into dexterous hands. The sensor extended the perception surface from a single side to multiple sides. The robotic fingers and the contact body cannot provide a grasping force similar to that of the rigid hand. Therefore, enlarging the ratio of solution B (A/B ratio 1:15) can reduce the hardness and enhance the deformation of the contact body. Taylor et al. [75] designed a compact fingertip tactile sensor, and the rigid structure provided enough clamping force. The hardness of the contact body was increased to adapt the grasp by decreasing the ratio of solution B (A/B ratio 1:10). Considering lower spatial resolution, Donlon et al. [6] adjusted the mixture ratio to 15:1 to obtain a stiffer and more elastic contact body. Wilson et al. [76] designed a 2-DOF manipulator composed of multiple Gelsight sensors with higher stiffness than [74].



**TABLE I**  
TYPE OF SILICONE USED FOR THE PREPARATION OF THE CONTACT BODY

Silicone brand	Model	VBTS	Representative work / Year	Color	Mixing ratio	Hardness	Cure method	Cure time	
Silicones	XP-565	Gelsight	Romero et al. [74] / 2020	Transparent	1:15	5A-20A	Standing	16h~18h	
			She et al. [61] / 2021		1:15~3				
			Wilson et al. [76] / 2022		18:1				
		Gelslim	Taylor et al. [75] / 2021		1:10				
			Donlon et al. [6] / 2018		15:1				
			Gomes et al. [62] / 2020		1:22				
		FingerVision	Yamaguchi et al. [63] / 2019		—				
Smooth-On	Solaris™	Du et al. [65] / 2021		Transparent	1:1	15A	Standing	24h	
	Sorta-Clear™ 12	Soter et al. [67] / 2019		Water white	1:1	12A		12h	
	Sorta-Clear™ 18	Kappasov et al. [68] / 2019			1:1	18A		24h	
	Dragon Skin™ 20	Yu et al. [69] / 2020		Translucent	1:1	20A		4h	
	Ecoflex™ 50	McInroe et al. [70] / 2018			1:1	00-50		3h	
	Ecoflex™ GEL	Huang et al. [71] / 2020			1:1	000-35		2h	
	Vytaflex™ 30	Soter et al. [73] / 2020	Off-White	1:1	30A	16h			
	Vytaflex™ 60	Sun et al. [102] / 2022		1:1	60A	16			
		Ward-Cherrier et al. [50] / 2018							
WACKER	ELASTOSIL ®	Sferrazza et al. [66] / 2019		Colorless	7:1	45A	(150°C)	30min	
	RT 601 RTV-2	Griffa et al. [129] / 2022			25:1	10A			
	SiGel® 612	TH-Tactile	[8] ~ [15] / 2018~2022		Clear	1~1.7:1			10A
Techsil	RTV27905	Tactip	[50] / 2018	1:1		00-10	(25°C)	20h	
				(100°C)		1h			
Tango Materials	Tango Black+	Tactip	[50] / 2018	Black		—	26~28A	3D print	—
Dow	SYLGARD DC184 PDMS			Yang et al. [89] / 2021	Colorless	10:1	43A	(25°C)	48h
								(100°C)	35min
								(125°C)	20min
							(150°C)	10min	

Hence, it enhanced the hardness (adjusting the ratio to 18:1) to avoid excessive deformation.

In addition, researchers have also tried to add other reagents to improve the quality of silicone. She et al. [61] mixed the dilute agent (LC1550 Phenyl Trimethicone, Lotioncrafter) with silicone in a ratio of 3:1:15. The dilute agent improved the softness and elasticity of silicone. Similar works included [6] and [74] using NOVOCS silicone dilute agent from Smooth-On Company. Gomes et al. [62] also added Slacker<sup>1</sup> (Smooth-On) to the silicone solution in a ratio of 22:1:22. Slacker contributed to the tackiness of silicone. A sufficient Slacker can improve the contact body's ability to capture high-frequency imprints.

**2) Preparation:** Modifying the preparation process can improve the quality of the contact body. We conclude the general preparation process of a single silicone layer, as shown in Fig. 3(a). First, the silicone solution is poured into the beaker according to the proportion with strict error control. Second, the solution is evenly stirred in the same direction. Then, they are poured into the mold and placed in a vacuum environment [77] for static removal of bubbles (some silicone solutions can automatically precipitate bubbles). Finally, static curing or heating curing is selected according to the curing time. For some silicone, another effect of heating is to strengthen the formation of molecular bonds. For instance, heated WACKER SiGel 612 has a higher hardness and lower viscosity than naturally cured silicone. The preparation of elastic skin is slightly different from that of the contact body [78], [79]. As shown in Fig. 3(b), silicone solution is poured into the base mold in advance. When combining two

molds, the static pressure generated by the sticky silicone solution retains a gap until the film forms.

Compared with a single silicone layer, a composite silicone layer can achieve the integration of various silicone properties. Sferrazza and D'Andrea [66] proposed a multilayer silicone preparation method, as shown in Fig. 3(c). The first layer was a high-hardness transparent silicone (ELASTOSIL<sup>1</sup> RT 601 RTV-2: mixing ratio: 7:1 and shore hardness: 45 A). Then, a soft silicone layer (Ecoflex GEL: mixing ratio: 1:1 and shore hardness: 000–35) was fabricated above the first layer. Finally, a layer of silicone with a medium level of hardness (ELASTOSIL RT 601 RTV-2: mixing ratio: 25:1 and shore hardness: 10 A) was cast.

Silicone fabrication has a low fault tolerance rate. The errors cause batch differences in the contact body, while 3-D printing technology can improve preparation precision. Pestell et al. [80], [81] used rapid prototyping technology with an Object 3-D printer to create the flexible skin of the Tactip sensor with TangoBlack+. 3-D printing speeds up the preparation and increases the possibility of adding complex features to the contact body. However, the printing technology of transparent silicone is immature, so researchers prefer to prepare transparent silicone by casting. Without considering the shape and performance of silicone, the commercial contact body [82], [83] is also a feasible scheme because of its high interchangeability.

## B. Marker Layer

**1) Marker Type:** The marker types are related to the force properties. The single-layer marker can present the slipping direction and magnitude. However, the representation of the normal force is insufficient, resulting in its maximum error in 3-D force estimation [49].

<sup>1</sup>Registered trademark.

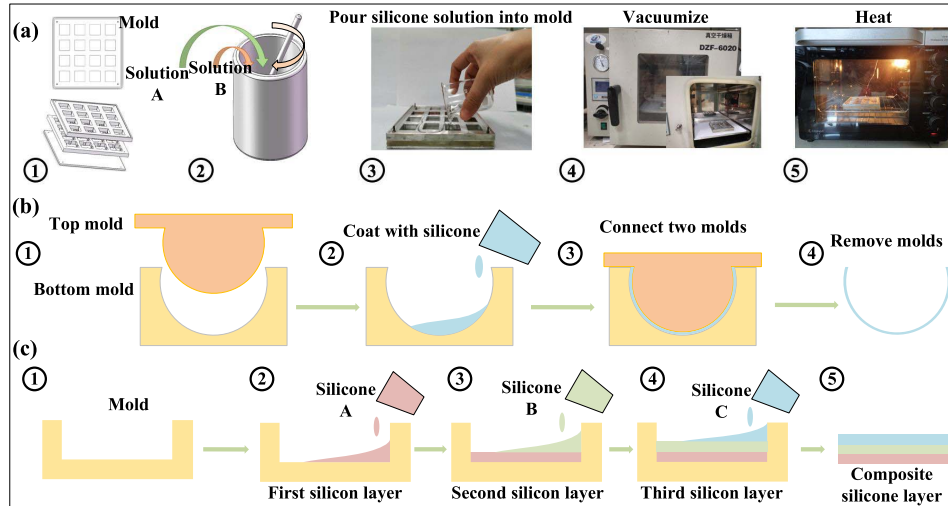


**Fig. 3.** Preparation of contact body. (a) Preparation process of elastomer: ① multiple molds are assembled and fixed; ② silicone solution is mixed according to the proportion and evenly stirred in one direction; ③ mixed solution is poured into the mold; ④ it is placed in a vacuum environment for the static removal of bubbles; and ⑤ it is cured by heating. (b) Preparation process of an elastic skin/film. Under static pressure, there is a gap between the two molds to form a film. (c) Preparation process of a composite silicone layer. Different types of silicone are poured into the mold in turn to solidify. The composite silicone layer can achieve the integration of various silicone properties.

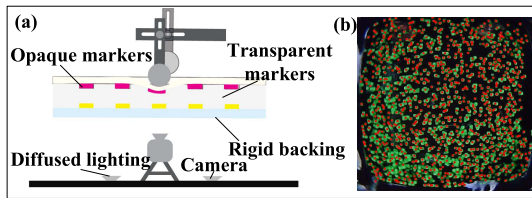


**Fig. 4.** (a) Overlapping colors and region displacement represent the force distribution [84] (2019 IEEE). (b) Random markers adopt key points as [66] (got copyright permission from MDPI).

For the single-layer marker, the errors of image processing are easily confused with the area variation. The multilayer marker layer can provide distinct spatial differences, as shown in Fig. 4(a). In [84], two layers of marker array were inside the contact body, where the upper layer was a magenta flexible marker layer, and the lower layer was a yellow rigid marker layer. Under pressure, the area of magenta markers was increased and overflowed from the overlapping regions (the overlapping color of yellow and magenta was red). When subjected to shear force, the overlapping area shrunk as the yellow marker overflows. The correlation between marker area and stress was beneficial for improving the estimation precision.

Ouyang and Howe [85] replaced the marker array with a specific marker pattern. The motion of the reference point can be used to deduce the forces and torques applied to the sensor. Li et al. [24] simplified the three-axis force presentation via three markers with a triangular distribution. Yu et al. [69] used strip markers with alternating color. It detected pressure by tracking the bending and deviation of the line. We think that these single marker modes limit the acquisition of multi-tribute forces compared with the marker array.

**2) Marker Attribute:** The marker shape, density, and size are also related to the recognition effect. The circle is a commonly used marker shape in VBTS. Lin and Wiertelowski [84] adopted square markers. However, the marker center produces

measurement errors during tilting. Hence, in [86], the round marker was reintroduced in the improved sensor.

Each marker corresponds to the fixed regions to capture the deformation state. Theoretically, increasing the marker density will expand the effective recognition regions and enhance the sensitivity. As reported in [85], markers with low density and large area were unable for local tactile calibration, especially in locating contact positions. However, the high density of markers increases difficulties in image processing. The fluorescence particle [66] and the random pixel pattern [65], [87] adopted the center point or key point of the local regions as a reference [see Fig. 4(b)]. Although interpolation was not required to match all markers, it is easy to miss the initial tactile information. The dense markers may affect texture representation when simultaneously capturing texture and force. Therefore, researchers set the spacing between markers, such as 1~3 mm [48], [82]. According to the tactile afferent density of human fingertips (140/cm<sup>2</sup>), Cui et al. [41] set the spatial resolution as 0.9 mm.

The Robotics Team from the University of Bristol adopted 3-D printing to explore the optimal sizes [69]. Most of the time, it is difficult to obtain an optimal size and density of markers due to the limitations of experimental conditions. Therefore, the size setting is required not to affect the representation of tactile features. The Gelsight sensor initially adopted random markers, but the later versions updated them to the mesh distribution. We think that there are some missing markers during image processing, so the regular distribution can accurately fill these markers. In addition, Ma et al. [64] regarded the mesh as the FEM nodes to reconstruct the contact force distribution.

**3) Marker Preparation:** The preparation materials of the markers include silicone solution, printing ink, colored powder, and paint. We summarize four preparation methods as shown in Table II.

TABLE II  
COMPARISON OF FOUR FABRICATION METHODS OF THE MARKER LAYER

Preparation scheme	Preparation method / Year	Material	Advantage	Limitations	Application
Printing on the surface	Laser etching and spray painting [76] / 2022	Silicone paint	High stability	High cost; Complex preparation process	Sliding detection
	Print markers with template [88] / 2020	Balloon screen printing ink	Simple preparation process; Low cost	Thickness influence; Low precision	
	Mark with UV pen [83], [130] / 2020, 2022	Ultraviolet ink	Simple preparation process	Lower precision	
Separate fabrication	Water transfer paper [41] / 2021	Toner	Simple preparation process; Low cost; Convenient for marker design; High precision markers	Cause marker layer to wrinkle	Sliding detection
	Random color pixels pattern [65] / 2021	—	Simple preparation process; Low cost; High precision markers	Standardize markers; Cause marker layer to wrinkle	
	Plastic beads [89] / 2021	Plastic	High stability; High precision markers	High cost; Complex preparation process	
Fabrication inside contact body	Mixed filling [69] / 2020	Silicone and dye	Simple preparation process; Low cost	Low density; Low-resolution	Normal force detection
	Randomly adding markers [66], [132] / 2019	Particles	Simple preparation process	Standardize markers	
	Compound preparation [84] / 2019	Silicone and dye	High contrast signal;	Complex preparation process	
Integration fabrication	3D print [50] /2018	Tango Black+ and dye	High stability; High precision markers; Convenient for marker design	High cost; Complex preparation process	

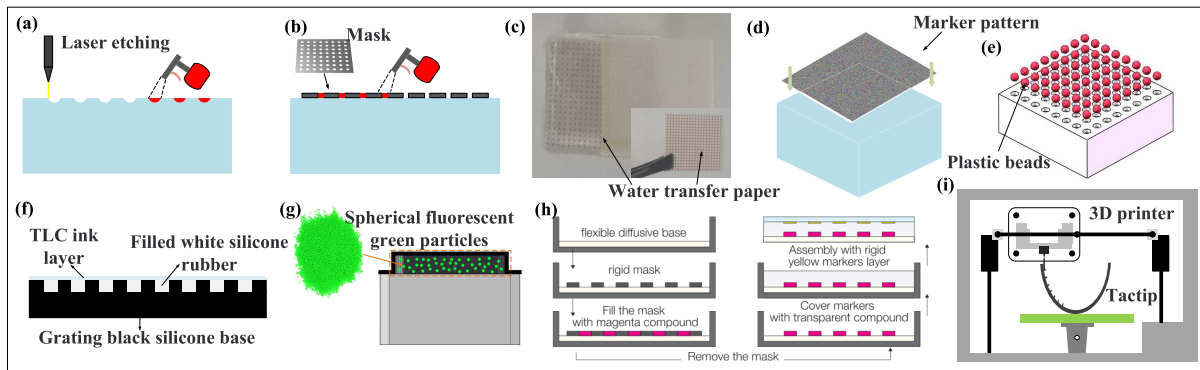


Fig. 5. Four types of marker preparation. (a) Laser etching locates marker holes and then sprays paint. (b) Spray paint on the template to print markers. (c) Attach water transfer paper to the contact surface to print markers. (d) Stick a semitransparent pattern of random color pixels on the contact surface. (e) Embed plastic beads in the holes. (f) White silicone is filled into the grooves. (g) Spherical fluorescent green particles are mixed into the contact body [66] (got copyright permission from MDPI). (h) Two marker layers are separately fabricated inside the contact body [84] (2019 IEEE). (i) 3-D printer prints tip and pins.

- 1) *Printing on the Contact Surface*: Wilson et al. [76] printed markers on the contact surface by laser etching and spray paint [see Fig. 5(a)]. Taylor et al. [75] cut small holes on the contact surface by laser and painted black silicone ink. Kuppaswamy et al. [88] attached a mask plate on the contact body [see Fig. 5(b)]. The balloon screen printing ink was cast into the template to print the markers. The thickness of the template determined the thickness of the marker layer. The thicker marker layer causes cracks after the reflective layer is attached. Abad and Ranasinghe [83] used a COTS UV pen and ultraviolet (UV) ink to directly mark UV markers on the contact surface.
- 2) *Separate Fabrication*: Cui et al. [41] printed the marker pattern on water transfer paper by a laser printer [see Fig. 5(c)]. Then, a marked side was attached to the con-

tact body and wetted from the back. After transferring the marker layer, the paster was removed. Du et al. [65] printed a semitransparent pattern of dense random color pixels [see Fig. 5(d)]. There is an RGB difference of more than 30 between the adjacent pixels. Yang et al. [89] left the positioning holes on the contact surface. The plastic beads were embedded in the holes and heated at high temperatures to form a hard silicone shell with an internal marker array [see Fig. 5(e)].

- 3) *Fabrication Inside the Contact Body*: Yu et al. [69] filled a mixture of silicone solution and white dye into the grooves on the inner surface of a black silicone base [see Fig. 5(f)]. In [66], spherical fluorescent green particles were mixed with silicone solution to pour into the mold [see Fig. 5(g)]. The solidified contact body contained random markers inside. Lin and Wiertelwski [84]

TABLE III  
COMPARISON OF SEMISPECULAR AND MATTE COATINGS

Reflective layer type	Material	Advantage	Limitations
Semispecular coating	Copper flake or aluminum flake paint	Higher reflective performance; Higher sensitive; Higher contrast signal	High cost; Complex preparation process
Matte coating	Aluminum powder, silicone ink, black silicone paint, silver paint, color powder-silicone	Lambert reflect; Accurate measurement of general shape; Low cost; Low preparation difficulty	Low reflective performance

TABLE IV  
COMPARISON OF FOUR FABRICATION METHODS OF THE REFLECTIVE LAYER

Preparation method	Material	Advance preparation	Attached form	Uniformity	Preparation difficulty	Cost	Abrasion resistance
Coating	Silicone paint; Powder; Ink	Covering silicone adhesive in contact body	Mechanical adhesion	Low	Low	Low	Medium
Spraying		Adding silicone and silicone base		Medium	Low	Medium	Medium
Sputtering	Metal (Al, Cu)	—		High	Medium	High	Low
Improved process [97]	Silicone paint; Powder; Ink	Covering release agent and chemical reagent in module; Adding silicone and silicone base	Chemical adhesion	Medium	High	Medium	High

fabricated two marker layers inside the contact body, as shown in Fig. 5(h). The first layer was a white light-diffusive soft layer, under which a rigid template was placed on the first layer to print magenta markers via screen-printing. After removing the template, they were covered with transparent compounds and bonded with the rigid yellow marker layer.

- 4) *Integration Fabrication*: Researchers designed an integration mold to fabricate the contact body and the markers or printed them with a 3-D printer [see Fig. 5(i)] [50]. In addition, the top of the pins was coated with white paint to enhance identification. Stone et al. [90] replaced regular coatings with phosphorescent paint to reduce the need for continuous illumination.

### C. Reflective Layer

The reflective layer should be an even, thin, smooth, and firm membrane attached to the contact body. The fineness and thickness affect the tactile sensitivity and the presentation of fine details on objects. Uneven reflective layers also increase the noise of tactile images.

1) *Reflective Layer Material*: The reflection performance is related to the material of the reflective layer. Yuan et al. [48] introduced two types of coatings (see Table III). One was a semispecular coating made of copper flake or aluminum flake paint [74], and the other was a matte coating made of aluminum powder [91]. The matte coating is a Lambert surface for the measurement of the general shape. Similar matte coatings include silicone ink (print-on silicone ink) [75], [92], black silicone paint [73], silver paint [65], and a mixed coating of color powder and silicone [62], [93].

The semispecular coating is sensitive to microgeometry on the normal. Hence, it can provide a higher contrast signal than matte coatings. In addition, there is a small amount of diffused light on the specular surface, while the Lambert surface completely diffuses light. Since the light does not dissipate, it maintains directionality to illuminate the deformation surface more uniformly. There are some other types of

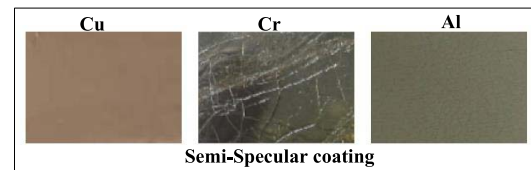


Fig. 6. Three types of metal materials are tested for semispecular coatings. Cu can provide a fine and uniform surface, but Al and Cr exhibit uneven regions or crack.

reflective layers. For example, the black silicone layer and the temperature perception layer [94] can act as a reflective layer to block external light [95].

2) *Reflective Layer Preparation*: The specular coating has higher requirements for fineness and smoothness than the matte coating. Painting (see Table IV) is the simplest method to fabricate a reflective layer [65], [91] but with low uniformity [see Fig. 7(a)]. In [75] and [83], a customized miniature spray can be used to spray the paint on the contact surface through high pressure [see Fig. 7(b)]. Although there were some thickness differences, they can form a local uniform coating. Another method is depositing an aluminum/copper membrane by a sputtering process [96] [see Fig. 7(c)]. It can obtain a high-quality coating, but the poor combination of the metal material and silicone causes low wear resistance [see Fig. 6(b)]. Therefore, VBTs require replacing the contact body regularly, which indirectly increases the maintenance cost.

Since silicone is hard to adhere to other materials, the above process needs to add silicone and silicone base into the paint or coat silicon adhesive on the contact surface. These reagents can enhance the adhesion between the coating and silicone. In addition, researchers added dilute agents, such as NOVOCS silicone dilute agent [75] and Novocs TM Matte [83], to reduce coating viscosity. However, the excessive solvent ratio will lead to wrinkling of the reflective layer.

In [74], the results indicated that the reflective layer with mechanical attachment was not firm. Hence,



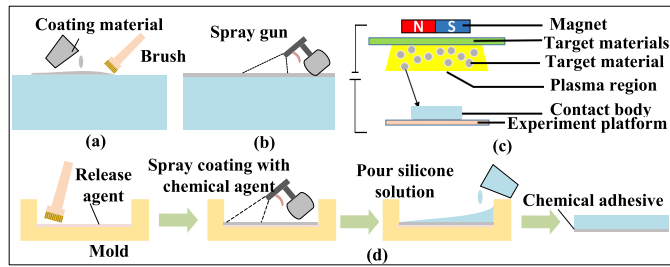


**Fig. 7.** Preparation process of the reflective layer. (a) Brushing paint on the contact surface is the simplest approach to fabricating a coating. However, it has low uniformity. (b) Spraying is an effective method to improve uniformity, but it depends on the skill and feel of the operator. (c) We prefer the sputtering process because it can provide a smooth coating. It has a limitation in durability because of low adhesion between metal and silicone. (d) Preparation process of chemical adhesion. The uncured paint and silicone form a strong chemical bond to improve adhesion.

Romero et al. [74] and Lambeta et al. [97] developed a new manufacturing process to improve the coating adhesion, as shown in Fig. 7(d). First, the release agent and spray silicone paint were smeared on the mold. Then, a chemical reagent (Dow DOWSIL P5200) was added to create a reflective layer with uniform thickness. Finally, the silicone solution was poured into the mold when the paint was uncured. It formed a strong chemical bond between the coating and the contact body. Although the process is complicated, the idea of chemical adhesion is worth exploring.

#### D. Protective Layer

The reflection layer of most sensors is in direct contact with the objects. The low wear resistance of the reflective layer limits the protective effect [see Fig. 8(a)]. Therefore, a protective layer is attached to protect the reflective layer and the contact body. However, an additional layer may affect the deformation sensitivity of the contact body, so the protective layer should be as thin and hard-wearing as possible as shown in Table V.

Initially, nonsilicone coatings were tested as a protective coating [6], but they would not stick to the contact body effectively. In contrast, silicone materials had a stronger adhesion with a reflective layer or contact body [65] [see Fig. 8(b)]. Researchers have also tested various types of filled and unfilled silicone [6]. The filled silicone covering the surface of the specular coating increases the thickness of the functional layer and, thus, increases the impedance. However, the sensitivity of pressure detection is less affected by the silicone protective layer. The thin silicone protective layers are rubbed off after hundreds of grasps, indicating that they are not effectively attached to the contact body.

Compared with the silicone protective layer, the stretchy and loose-weave fabric [6], [64] can provide better contact protection and increase signal strength [see Fig. 8(c)]. The fabric textures reduce the contact area between the object and the sensor. VBTs can detect flat features by increasing the pressure to the point. In addition, when grasping an untextured object, the signal of the contact body without a protective layer is low, while fabric can enhance the contact signal. In addition, Wang et al. [92] considered the feasibility of medical tape

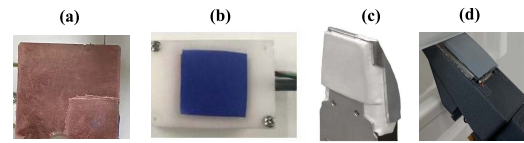


**Fig. 8.** Four types of reflective layer materials. (a) Reflective layer as a protective layer can reduce the thickness of the function layer [15]. (b) Silicone layer covers the contact surface to protect the contact body [10]. (c) Ma et al. [64] (2019 IEEE) used fabric to provide contact protection and increase signal strength. (d) Medical tape has smooth and sensitive characteristics to retain a lower coefficient of friction with more contact detail [92] (2021 IEEE).

**TABLE V**

**COMPARISON OF FOUR TYPES OF PROTECTIVE MATERIALS**

Material	Thickness	Sensitivity	Protection
Reflective layer	Very thin	Higher	Worse
Silicone	Thick	Low	Higher
Fabric	Medium	Medium	High
Medical tape	Thin	High	Medium

(3M Tagaderm) [see Fig. 8(d)]. The smooth and sensitive characteristics retained a lower coefficient of friction with more contact detail. Although it is not suitable for grasping heavy objects, it can provide a medium level of protection to perform routine detection or motion tracking (see Table V).

#### E. Other Function Layers

The temperature perception layer is made of temperature-sensitive materials [10], [94], which are characterized by different colors at different temperatures. As a result, VBTs can obtain temperature information through color tracking.

Xiang et al. [82] added a conductive, soft, and stretchable EA layer (J-Flex, U.K.). It was a symmetrical EA electrode pattern with an electrode width and space of 5 mm and an effective electrode diameter of 125 mm. The EA layer provided electrostatic attraction forces for VBTs to improve effective contact with objects.

#### F. Supporting Structure

The contact module requires a supporting structure to fix inside the sensor. The external supporting structure is the frame of the sensor, printed with resin or nylon by a 3-D printer. The internal supporting structure requires direct contact with the underside of the contact body. A high transparency supporting structure can ensure that the camera detects the deformation of the contact body. Acrylic materials are commonly used for intersupporting structures, such as acrylic plates [65], acrylic sheets [69], acrylic tubes [93], acrylic thin shells [74], and acrylic windows [97], as shown in Fig. 9.

Regular shapes of acrylic as standard parts can be purchased from suppliers or customized in a batch. Manual preparation may appear with a rough edge and surface cracks in the cutting process. In [6], stress cracking occurred on the edge after contact with a solvent. These cracks destroyed the optical continuity of the acrylic sheet. Therefore, annealing was adopted to eliminate stress to ensure transparency. In addition, acrylic components can be fabricated by a 3-D printer [74], which improves the precision and avoids damage caused by secondary processing.



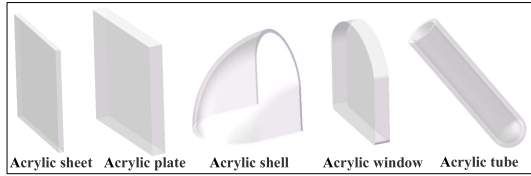


Fig. 9. Different shapes of supporting structures fabricated by acrylic.

The acrylic was also replaced with standard quartz blocks considering the high-temperature resistance [8]. A quartz block is first placed at the bottom of the mold. Then, silicone is filled into the closed area above it. After curing, the contact body sticks firmly to the quartz block. Integrated preparation ensures transparency of the connection between acrylic and quartz blocks. Another one is separately fabricating the contact body and using transparent silicone adhesive to adhere it to the quartz block.

### G. Summary of Contact Module

The selection of the silicone model first considers the form of the contact body. The elastic skin relies on high hardness silicone to support the structure. The elastomer requires hardness to adapt to the grasping force to maintain sufficient sensitivity. On the one hand, it is difficult for the far softer contact body to reflect the depth difference of the large deformation. On the other hand, high-hardness silicone cannot provide effective deformation to map contact features. Most silicone is configured with the standard hardness. Adjustable silicone can obtain any hardness in the reference interval, and the optimal ratio is inferred through the iterative method.

Excessive additives affect silicone properties. For instance, the colored powder makes the contact body generate many pores after curing. When decreasing the viscosity of the silicone solution, the powder will precipitate in the process of silicone standing, resulting in the uneven color of the contact body. In addition, the diluents and reinforcers can modify silicone, but the imbalance of proportion will damage performance.

The silicone color is also a nonnegligible factor because it is closely related to the final color or transparency of the contact body. The transparency determines the imaging clarity. First, silicone cleaning and bubble removal must be ensured in the preparation process. Since stirring causes air to enter the silicone solution to form bubbles, it requires stirring the silicone solution in the same direction and placing it in a vacuum environment. In addition, the precision of the mold surface is as high as possible to prevent the formation of a rough silicone surface. Finally, the supporting structure should adopt transparent material and adhere to the contact body with transparent silicone adhesive, such as Smooth-On Sil-Poxy [76] or A-564 Medical Silicone Adhesive [92].

Another influencing factor of imaging is the reflective layer. Quality is estimated according to four indicators: reflectivity, uniformity, thickness, and density. The uniform and thin reflective layer can minimize the influence on the sensitivity of the contact body. Hence, it should be made of fine particles so that the coating can reveal the finer details of the object. The

fine particles ensure a reliable shading effect of the reflective layer, while coarse particles, even if uniformly covered, still have light leakage that causes excessive noise. Metal materials reflect better than silicone paints (ink) or color powders with relatively high costs. The specular coating has a higher spatial resolution than the matte coating under the same materials.

Compared with in-body markers, surface markers have the advantage of slip detection. The multilayer marker layer has a better presentation of the normal force than the single-layer marker. The thickness of the functional layer restricts the number of marker layers, while there is no limitation inside the contact body. In addition, the superposition of function layers may cause the overlap of feature regions. If the marker layer decreases the marker spacing, the other tactile information is lost. It also increases the difficulty of image processing and recognition. Abad and Ranasinghe [83] proposed a UV marker that can realize the arbitrary conversion of texture and marker regions under the control of ordinary and UV LEDs. In [15], the regional distribution was adopted to avoid mutual influence.

With the increase in functional layers, even if each layer is thin, there is a superimposed effect on sensitivity. Therefore, the reflective layer sometimes acts as a protective layer to reduce the layer thickness. Limited by the material characteristics, it is easier to improve adhesion than wear resistance, such as chemical adhesion. Many VBTSs are also equipped with specific protective layers to increase durability. The balance of protection and sensitivity depends on the bias of demand.

## IV. ILLUMINATION MODULE

### A. LED Type

The LED combinations can provide more uniform illumination than a single LED [98]. The initial Gelsight sensor adopted an independent LED design. Driven by the modular design, LEDs were integrated into the circuit boards. There are three circuit board styles: square, strip, and ring. Werner et al. [99] adopted a square LED panel with a hollow in the middle for mounting the camera. Pestell et al. [80] used a PCB ring consisting of six LEDs to illuminate the interior of the tip. James et al. [37] embedded four LEDs on two PCB strips and mounted them on the upper part of the sensor along the axis. Fernandez et al. [100] customized a PCB ring containing sixteen LEDs. The eight downward-facing red LEDs enabled the camera to track fingertip movements, and eight upward-facing blue LEDs infused blue light into the dome waveguide. To lessen the size of the PCB, Cui et al. [41] adopted a flexible LED strip. The LEDs integrated into the PCB board effectively reduce the wire arrangement. The LED brightness is usually constant, but some researchers manually controlled the brightness with PCBs and controllers. In [97], the illumination module provided a maximum brightness of 4 lm.

### B. Light Color

To present the deformation gradient, researchers designed a polychromatic illumination scheme in GelSight [19] and built a gradient table to reconstruct photometric stereo. The hue and

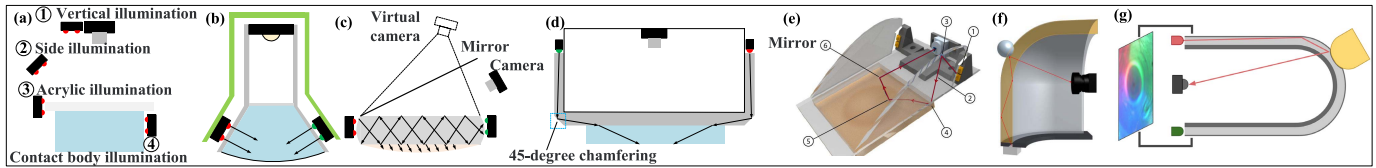


**Fig. 10.** LED position and optical path design. (a) There are four methods of illumination. Vertical illumination is limited by the sensor size. Side illumination causes edge regions to lack brightness. Acrylic and contact body illumination can provide uniform light through TIR. (b) and (c) Light is refracted through the acrylic plate into the contact surface [19]. (c) Mirror is used to change the light direction [92]. (d) 45° chamfering is used to change the direction of the refracted light [28]. (e) Donlon et al. [6] (2018 IEEE) adopted the parabolic reflection principle and TIR to plan an optical path. (f) [74] (2020 IEEE) and (g) [62] (2020 IEEE); TIR is performed inside the contact body. The deformation causes a change in the optical path.

saturation of each pixel indicated the direction of the surface normal. The color intensity contained the magnitude of the gradient change. In recent years, some work has focused on the improvement of reconstruction precision [74], [92].

Many VBTSSs followed this illumination design but adjusted the light color and the LED position. Hogan et al. [101] placed four LEDs with red, green, blue, and white colors on four sides of the contact body. Li et al. [24] placed tricolor LEDs (red, green, and blue) at intervals of 120° in a hexagonal sensor. In [92], the tricolor LEDs (red, green, and blue) were distributed at intervals of 90°. In [102], tricolor LEDs were distributed alternately at intervals of 45° to illuminate the finger cavity. These instances adopted at least three colors. This ensured that each dimension had a superposition of more than two colors. In [74], the asymmetric light color resulted in the lack of partial gradient information.

Without 3-D reconstruction, Donlon et al. [6] adopted a pair of high-energy neutral white LEDs (OSLON SSL 80) on either side of the finger to project the light onto the contact body. Sometimes, light color is related to light diffusivity. In [84], white light was scattered by background or magenta markers. The scattered light was filtered through a yellow filter. Patel et al. [103] replaced green and red LEDs with fluorescent paints. Six blue LEDs excited the paint to emit polychromatic light. In addition, special light, such as UV light [83], was used for illumination and marker display.

### C. LED Position

In Fig. 10(a), vertical illumination is an ideal illumination method. For example, Jiang et al. [96] placed four white LEDs above a camera. LEDs are also in the same plane as the camera. In [99] and [104], LEDs were regularly distributed around the camera to provide vertical illumination. The second illumination method is side illumination (see Table VI). Tactip [50] placed an LED ring on the upper lens or both sides. Compared with vertical illumination, this illumination mode enables the central regions of the contact surface to be bright, but the edge regions lack brightness. To reduce uneven illumination, researchers adhered LEDs to the sides of the contact body or supporting structure, as shown in the third and fourth methods in Fig. 10(a).

### D. Optical Path Design and Light Source Optimization

1) **Optical Path Design:** As the sensor size decreases, the narrow space cannot perform vertical illumination. Therefore,

**TABLE VI**  
COMPARISON OF ILLUMINATION POSITIONS

Form	Optical design	Advantage	Limitations
Vertical illumination	No	Simple illumination; Uniform illumination	Large space
Side illumination	No	Reducing illumination space	Inadequate illumination
Acrylic/Contact body illumination	Yes	Uniform illumination of micro VBTSSs	Optical path design

researchers have paid attention to the design of light paths. The supporting structure has been the optical element involved in light transmission. In [92], the acrylic plate refracted light into the interior. Some light continued to travel within the acrylic, while the other light was refracted into the contact body to illuminate the whole contact surface [see Fig. 10(b) and (c)]. Luo et al. [20] cut an acrylic plate into a semibox-shaped sheet. The LEDs were attached to the edge of the acrylic surface. The 45° chamfering was machined at the sheet bottom to change the direction of the refracted light [see Fig. 10(d)]. In [6], a wedge-shaped sensor relied on acrylic sheets on both sides to design a more accurate light path [see Fig. 10(e)]. The acrylic sheet was designed as a parabolic shape, where LEDs were at the focal point to provide illumination. The scattered light was converted into parallel light using parabolic reflection. Because acrylic had a higher refractive index than air, the light was totally reflected inside the acrylic when the incident angle was larger than the critical angle [namely, total internal reflection (TIR)]. Through the 90° reflection mirror at the acrylic bottom, the parallel light refracted from the acrylic bottom to the contact surface.

TIR inside the contact body can reduce optical loss. In [74], there was a fingertip-shaped contact body whose inner surface is attached to the thin acrylic shell [see Fig. 10(f)]. Light entered from the bottom edge of the contact body. Because the refractive index of silicone was higher than that of air and acrylic, light was reflected inside the contact body. The deformation of the contact surface caused the light to change direction. The camera received the reflection light and formed a tactile image. Similarly, inside a finger-shaped sensor [62], LEDs were mounted at the root of the finger. Light propagated inside the finger-shaped contact body via TIR [see Fig. 10(g)].

As shown in Fig. 10(c) and (e), the camera is on the side of the contact body [92]. Light is reflected off the mirror into the camera lens. Specular reflection reduces the imaging distance to maintain the compact sensor structure [6]. In addition,

Zhang et al. [105] used light refraction from four mirrors to realize virtual binocular vision. It enabled a monocular camera to capture 3-D tactile information.

**2) Optimization of Light Source:** Researchers have used optical elements to filter and concentrate light. Wang et al. [92] installed a gray filter and a diffuser between the LEDs and the acrylic plate. The light reflection inside the acrylic may decrease the contrast of the contact regions and the sensitivity of the surface gradient. The gray filter can absorb light to decrease lighting levels and internal reflection. In addition, the boundary regions lack adequate illumination, so the contact surface loses part of the gradient information. The diffuser can spread light smoothly over the entire contact surface and, thus, achieve more uniform global illumination.

Acrylic is fabricated as a lens to concentrate light and adjust the focal length. Taylor et al. [75] proposed the optimal design of acrylic lens shapes. They adopted a hexagonal prism as the initial lens geometry. In a simulated heatmap of radiation flux, there was some scattered light at the edges of the lens. The optimized lens improved the degree of light concentration by cutting multidimensional planes.

### E. Summary of Illumination Module

The illumination design considers the sensing function, the sensor size, and the reflective types. The scheme of polychromatic light can provide gradient information, so it is adaptive for 3-D reconstruction rather than marker tracking. The neutral light can visually present the geometric features, avoiding the extra noise caused by overlapping light. The brightness and light color should match the reflective types. The matte coating is suitable for Lambert reflection with polychromatic light, which can provide a stable and abundant deformation gradient. The specular coating is sensitive to brightness. Bright spots may appear under hard light. Vertical illumination is still the most effective illumination method without considering size limitations. Under a narrow space, TIR can alleviate the uneven light problem of side illumination, where the supporting structure will play a vital role in optical path design and light source optimization.

## V. CAMERA MODULE

### A. Webcam

The Gelsight sensor initially adopted a C310 camera from Logitech Company (71.15 mm  $\times$  31.3 mm  $\times$  25.95 mm) equipped with a 60° field of view (FOV) and a fixed focal length of lens [48]. It can capture 480 P resolution images at 30 frames per second (fps) via USB connected to a computer. The highest resolution was 1920  $\times$  1080. Abad and Ranasinghe [83] adopted a C270 camera with a size of 72.91 mm  $\times$  37.91 mm  $\times$  66.64 mm and a 55° FOV. It can adjust the focal length by rotating the lens. At 1.5 in from the object, the camera can still maintain imaging sharpness. Yang et al. [89] adopted a BRIO camera whose size was 27 mm  $\times$  102 mm  $\times$  27 mm. It had the advantage of high-definition imaging (capture images below 1080 P resolution at 60 fps) and autozoom control (5 $\times$  focus). Microsoft offers several commonly used webcams. In [73],

the Microsoft VX-1000 camera can capture 480 P images at 30 fps. It reduced the size to 2.06  $\times$  2.06  $\times$  2.46 in. Microsoft LifeCam Cinema [96] had a 5 $\times$  zoom and autofocus to avoid visual errors caused by manually adjusting the focal length. Webcam has the advantages of high-performance imaging, but its size is unsuitable for micro-VBTSSs.

### B. Microcamera

The microcamera is a modular camera that only retains image sensors and circuit boards. The ELP Company scaled down the microcamera to 40 mm  $\times$  40 mm, preserving the camera's standard FOV and imaging performance. Xiang et al. [82] adopted an ELP webcam 960 P (38 mm  $\times$  38 mm) with six types of imaging resolution. Below the highest resolution (1280  $\times$  960), the camera can capture images at 30 fps. It also had a 170° FOV and a 2.8-mm standard focal length. Sferrazza and D'Andrea [66] used an ELP USBFHD06H camera (38 mm  $\times$  38 mm) to capture images with seven types of resolutions. The standard focal length was 2.1 mm, and the maximum was 6 mm. The frame rate of the above cameras can meet the needs of static image acquisition, but it is unsuitable for dynamic tactile tracking. Hence, James et al. [106] used an ELP-USBFHD01M-L21 camera (38 mm  $\times$  38 mm) that had the highest acquisition rate of 120 fps below 720 P.

Fingervision requires embedding microcameras into finger-sized sensors. Raspberry PI has developed several miniature cameras with a size of 25 mm  $\times$  24 mm  $\times$  9 mm. They have the advantage of low price and high performance. In [6] and [92], researchers designed a compact wedge sensor using the Raspberry Pi Camera Module V1. It can capture 640  $\times$  480/320  $\times$  240 resolution images at 60/90 fps. The Raspberry Pi Camera Module V2 was the second generation of cameras, which updated the photosensitive chip to improve pixel and maximum resolution. The standard focal length was shortened from 3.6 to 3.04 mm. Short-range imaging can reduce the imaging space reserved by the sensor [65]. Raspberry PI also had advantages in the interchangeability of components, such as the lens and LEDs. In addition, the development board can integrate multiple functions, such as brightness adjustment and light color control.

In addition to the Raspberry PI cameras, there are some ultraminiature cameras, such as the Li-OV9712-USB-M8 camera (22 mm  $\times$  19.5 mm  $\times$  15 mm) [107], SYD (Misumi Electronics, 13.5 mm  $\times$  6 mm  $\times$  4.9 mm) [108], and Omnivision OVM7692 (3179  $\mu$ m  $\times$  2815  $\mu$ m  $\times$  2600  $\mu$ m) [97]. They have shined in the applications of microsensors and robotic finger vision. OVM7692 is currently one of the most miniature cameras. Benefiting from the ultraminiature size of OVM7692, Lambeta et al. [97] proposed a DIGIT sensor with a more compact fingertip structure and better overall size optimization (20 mm  $\times$  27 mm  $\times$  18 mm).

### C. Camera Lens

Cameras can adjust the optical parameters, such as FOV and focal length, through the interchangeable lens. For example, the wide-angle lens enhances the FOV to 150°~170° [106], [109], and the fisheye lens obtains an ultrawide FOV above



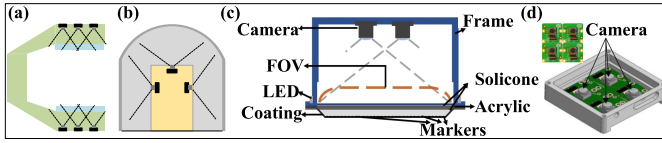


Fig. 11. Function of camera combinations. (a) Cameras are placed into a parallel gripper to cover the entire perception region [112]. (b) Cameras are spatially distributed to acquire global perception [91]. (c) Binocular camera is used to capture 3-D information [41] (2021 IEEE). (d) Four cameras can enlarge perception regions and provide 3-D information [104] (2020 IEEE).

180° [99], [110]. The noninterchangeable lens camera relies on additional lenses to adjust the optical parameters. The functions are given as follows.

- 1) Improve image quality. In [37], a nondistortion lens was connected to the JeVois machine vision camera system [67]. It can capture and process images of resolutions ranging from  $1280 \times 1024$  (15 fps) to  $176 \times 144$  (120 fps) using OpenCV.
- 2) Adjust the imaging distance. In [96], the robotic finger installed a micro-VBTS. The microlens and CMOS image sensor (CIS) provided a minimum object distance of 5 mm under limited space.
- 3) Expand the visual field. The lens can compensate for the visual field on the edge of the contact surface. In [111], the system adopted a wide-angle lens (2.1-mm focal length and 150° FOV) to capture the global marker array. In [96], a fisheye lens provided a wide visual field to capture the deformation state of the hemispherical contact surface.

#### D. Camera Combinations

Most VBTSs are equipped with a monocular camera. As the perception regions increase, it exposes the lack of visual field and spatial information. Hence, multiple cameras are adopted to enlarge the perception range and provide 3-D information.

- 1) *Enlargement of Perception Range*: We define the perceptual field as a plane and stereo field according to the spatial distribution of cameras. In [112], a parallel gripper installed a VBTS with multiple cameras. They were distributed in a plane to cover the entire perception region [see Fig. 11(a)]. In [109], two cameras were located at both ends of the cylindrical contact body to provide global coverage of the inner surface regions. The cameras with spatial distribution can provide an all-dimensional perception. Padmanabha et al. [91] embedded five cameras into the fingertip sensor, where four cameras were in a circular distribution, and one camera faced the fingertip [see Fig. 11(b)]. It comprehensively covered the fingertip and torus regions to acquire global perception.
- 2) *Provide 3-D Information*: A monocular camera only captures two-dimensional tactile information, while multiple cameras can provide depth information through the parallax. Cui et al. [41] adopted a binocular camera to capture contact information [see Fig. 11(c)]. 3-D tracking technology significantly improved the accuracy

in the contact point cloud, slip detection, and force estimation. In [104], an expanded sensing surface was presented through four cameras while 3-D tracking of marker movement [see Fig. 11(d)].

#### E. Camera Types

RGB cameras are commonly used in VBTSs. Professional cameras can adapt to specific perception tasks.

- 1) *Depth Camera*: It can directly form depth images instead of reconstructing the deformed regions, such as RGB cameras. For example, Li et al. [60] replaced an RGB camera with a depth camera to acquire accurate contour information. The depth information can also be used for posture estimation [57], human-machine contact interaction [71], and operational feedback [58].
- 2) *Event Camera*: It is a neuromorphic vision sensor inspired by a biological vision system that achieves fast response and high time-resolution imaging by tracking the intensity changes of each pixel. The dynamic tracking ability of the event camera significantly improves VBTSs to rapidly and continuously capture marker displacement [21], [113] and regional deformation [114].
- 3) *Infrared Camera*: Compared with temperature-sensitive materials, it can measure the accurate temperature. Wilson et al. [76] integrated an infrared camera into VBTSs to obtain the temperature distribution of objects. The robot can formulate the grasping strategy in advance through temperature feedback. In addition, Erickson et al. [115] adopted near-infrared spectroscopy and close-range high-resolution texture imaging to help robots interact and operate with the environment. An RGB camera with infrared LEDs and filters can achieve similar infrared imaging. However, the image quality is lower than that of an infrared camera [79].
- 4) *Endoscopic Camera*: As a special-size RGB camera, its slender shape is especially suitable for finger-shaped VBTSs [12]. Another notable characteristic is the built-in LEDs [90], which can manually adjust the brightness through the controller.

#### F. Summary of Camera Module

There are many types of commercial cameras for options as shown in Table VII. Researchers should focus on matching camera parameters with functional requirements rather than blindly pursuing camera miniaturization. Although microcamera performance has approached webcam, automatic focusing and high-speed acquisition are weak links. Because imaging distance fluctuates with the deformation of the contact surface, the fixed focal length may result in blurred images between frames, while autofocus ensures continuous clear imaging [23]. The high-speed acquisition can avoid frame loss, so dynamic tracking can sensitively capture tiny changes.

Cameras are equipped with multiple resolution modes. We think that 360 p~480 p are appropriate resolutions for VBTSs. The image resolution is inversely related to the acquisition frame rate. Capturing 360 p~480 p images at 30~60 fps can meet the requirements of real-time detection.



**TABLE VII**  
**CAMERAS AND OPTICAL PARAMETERS USED IN VBTSS**

Camera brand	Model	Size	Standard lens	Optional lens	Focal length(mm)	FOV	Resolution	Work / Year
Logitech	C270	72.91×37.91×66.64mm	Yes	No	Fixed focus	55°	720p/30fps	[83] / 2020
	C310	71.15×31.3×25.95mm				60°	480p/30fps 720p/30fps	[131] / 2021 [70] / 2018
	BRIO	27×102×27mm		Yes	Auto focus (5x)	90°/78°/65°	720p/1080p/4K 90/60/30fps	[89] / 2021
Microsoft	Lifecam VX-1000	2.06×2.06×2.46 inches	Yes	No	—	Wide-Angle	480p/30fps	[73] / 2020 [121] / 2018
	LifeCam Cinema	2.2×1.81×1.58 inches			Auto focus (100x)	—	720p/30fps	[96] / 2018
ELP	USBFHD01M-L21	38×38mm	Yes	Yes	2.1/2.8/3.6/6	150°/170°	480p/720p/1080p 120/60/30fps	[106] / 2020 [21] / 2020 [109] / 2020
	USBFHD06H				2.1/2.8/3.6/3.7/6	170°/180°	480p~1080p/30fps	[66] / 2019 [129] / 2022
	USBFHD01M-L180				2.1/2.5/2.8/3.6/6	170°/187°	480p/720p/1080p 60/60/30fps	[99] / 2020
	USB100W05MT				2.1/2.5/2.8/3/6	170°	480p~1080p/30fps	[79] / 2019
Raspberry Pi	V1 camera	25×24×9mm	Yes	Yes	3.6	Horizontal:53.5° Vertical:41.41°	480p/90fps 720p/60fps 1080p/30fps	[76] / 2022 [74] / 2020
	V2 camera				3.04	Horizontal:62.2° Vertical:48.8°		[104] / 2020 [65] / 2021 [87] / 2021
	Other module	—			—	—	—	[92] / 2021 [6] / 2018 [75] / 2021
JeVois	—	1.7 cubic inches	Yes	Yes	2.8	Horizontal:65°	240p/60fps 480p/30fps	[37] / 2021 [67] / 2019
iniVation (Event camera)	DVS128	50×50mm	Yes	—	2.6/3.6/4.5/8/12/25	Horizontal/Vertical: 89.1°/70.8°/65.2°/59.3°/46.2°/35.5°/24.1°/11.7°	128×128	[113] / 2019
	DAVIS240	55.25×55.78mm			3.5/4.5/6/12	Horizontal:64.6°/52.3°/40.5°/20.9° Vertical:50.6°/40.4°/30.9°/15.7°	240×180	[21] / 2020 [114] / 2022
Omnivision	OVM7692	3179×2815×2600μm	Yes	—	1.15/1.10	64°/71.9°	480p/30fps 320p/60fps	[97] / 2020
Leopard imaging	LI-OV9712-USB-M8	22×19.5×15mm	Yes	—	2.35mm	106°/89°/49°	240p~720p/30fps	[107] / 2019
Misumi	SYD	13.5×6×4.9mm	Yes	—	1.50/1.523/1.55/1.83	Horizontal:81°/132°/78.3°/69° Vertical:50°/65°/48.4°/43°	240p/240fps 480p/120fps 720p/90fps 1080p/60fps	[108] / 2021
—	Endoscopic camera	—	Yes	No	—	—	480p/30fps	[90] / 2020 [12] / 2021 [11] / 2019
PMD (Depth camera)	CamBoard pico flexxx	68×17×7.35mm	Yes	—	—	Horizontal:62° Vertical:45°	224×171/45fps	[71] / 2020 [58] / 2019

In addition, as reported in [48], most programs only supported 360 p~480 p images. Finally, the image size determines the network parameter quantity, so it is recommended to use as small an image as possible without affecting the definition.

Noninterchangeable lens cameras require additional lenses to adjust the optical parameters. Modular cameras, such as the ELP and Raspberry PI, can support multitype lenses, which increases the camera's diversity and reduces the time to configure additional lenses. The modular design also facilitates the integrated development of multiple functions, such as wireless function and LED control [85]. Although RGB cameras can provide a variety of modalities at a low cost, their professional performance is inferior to that of infrared cameras, event cameras, and depth cameras. Camera combinations can

compensate for the lack of spatial information and perception regions. The integration of multitype cameras is expected to expand perception modalities. Accordingly, camera quantity increases the load of image processing. A higher performance computer is required to achieve real-time detection. Therefore, researchers should comprehensively consider camera size, function, performance, and cost [89].

## VI. SUMMARY OF PREPARATION PROCESS

This review article concludes with seven design goals to guide the formulation of the technical route. These goals depend on the application requirements of VBTSSs. The goals include sensor size, perception form, optical property, perception function, cost, imaging performance, and durability.

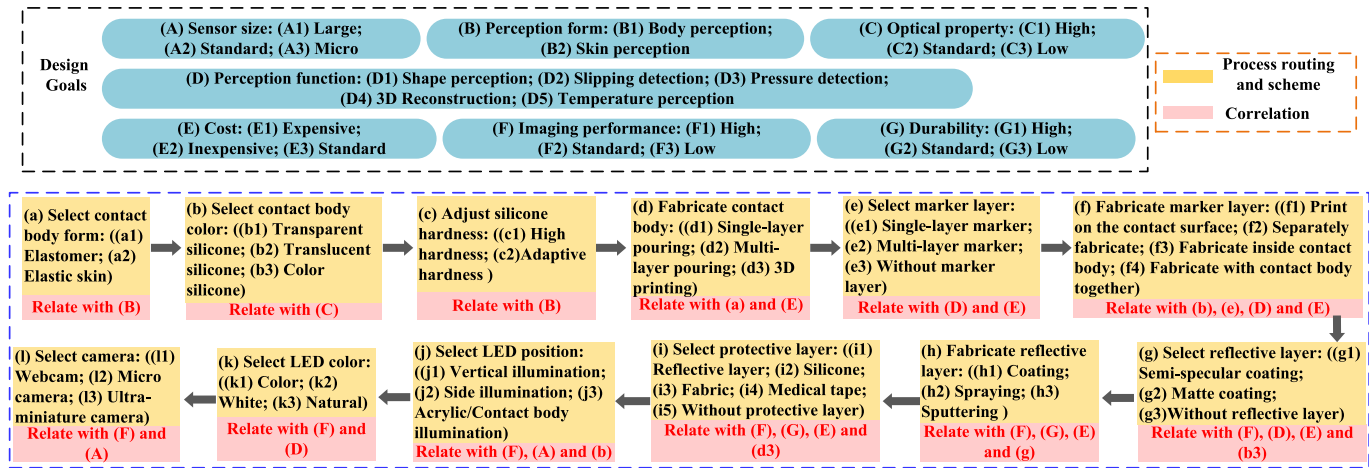


Fig. 12. Process flow diagram of VBTSs. We conclude with seven design goals and adopt a coding method to establish the correlation between preparation steps. A complete technical route is formulated by matching design goals to fabrication schemes.

In addition, we also consider the correlation between preparation steps. Hence, a coding method is adopted to establish a relationship between the preparation process, as shown in Fig. 12. We take an example of [15] to explain the process flow.

- 1) We set design goals: a micro-VBTS embedded into a soft hand requires microsize, body perception, high optical property, multimodal function (force, texture, and temperature detection), and high-performance imaging.
- 2) Accordingly, the contact body form is an elastomer, as shown in Fig. 12(a).
- 3) The high optical property requires transparent silicone, as shown in Fig. 12(b).
- 4) It adopts an iterative method to adjust the hardness to adapt to the grasp of a soft hand, as shown in Fig. 12(c).
- 5) Without the requirements of a multiattribute silicone layer, the single-layer pouring method is adopted to fabricate elastomers to reduce cost, as shown in Fig. 12(d).
- 6) A single-layer marker is enough to detect slip of contact surface, as shown in Fig. 12(e).
- 7) The markers are recommended to print on contact surfaces considering the contact body transparency, a single-layer marker layer, slip detection, and low fabrication cost, as shown in Fig. 12(f).
- 8) Because this sensor requires high imaging performance to map tactile information, the semispecular coating can provide high sensitivity and contrast, as shown in Fig. 12(g).
- 9) This sensor focuses on a high-performance semispecular coating, so metal sputtering can improve coating quality but with a high cost, as shown in Fig. 12(h).
- 10) Without considering durability, the reflective layer is used for protection to maintain high imaging performance, as shown in Fig. 12(i).
- 11) Limited by the sensor size, LEDs surround the acrylic/contact body's sides, as shown in Fig. 12(j).
- 12) Natural lighting is selected to avoid interference of color lighting, and it is beneficial for direct recognition of contact information, as shown in Fig. 12(k).

- 13) A microcamera just satisfies the size requirement, as shown in Fig. 12(l).

The specific scheme of each process step can be formulated and adjusted by referring to the cases summarized in Section II.

## VII. CHALLENGES AND FUTURE RESEARCH DIRECTIONS

### A. Keywords and Challenges

This article summarizes the development of VBTSs in recent years. Hardware technology has been developed in optimization design, material performance, and function development. However, it still faces the following problems and challenges.

- 1) **Durability:** According to the durability experiments [97], the contact body began to wear after repeated stress in a short period. Although researchers have been committed to searching for thin and wear-resistant protective materials, it is difficult to achieve a balance of wear resistance and sensitivity. The hardening problem of silicone also significantly increases the replacement frequency of contact bodies. Therefore, the durability of silicone will be one of the challenges for the commercialization of VBTSs.
- 2) **Interchangeability:** It is easy to ignore hardware interchangeability, resulting in errors from different manufacturing batches. The main errors arise from the inaccuracy of manual manufacturing. It also affects the generalization of the deep learning model based on the data drive. Although 3-D printing technology offers high-precision preparation, there is an urgent need for a fabrication breakthrough for transparent silicone.
- 3) **Assemblability:** Assembly errors may lead to recognition deviation. Enhancing assemblability facilitates sensor installation and disassembly and controls error. Assemblability and interchangeability improve sensor stability and utilization, indirectly reducing maintenance costs. However, establishing a standardized process is still a challenge.

- 4) *Sensitivity*: The sensitivity is closely related to tactile feedback. Limited by the elastic deformation mechanism, there is some hysteresis in the contact body. Improving the sensing mechanism and the material of the contact body is the key to alleviating the hysteresis problem.
- 5) *Multimodality*: VBTs have the potential for multimodal expression. However, the low degree of modal integration of the contact body limits multimodal development. Multisensor fusion is the basis of multimodal recognition. For VBTs, the camera is significant for modal development. Therefore, the combination of multitype cameras and functional layers is expected to improve the modal function.
- 6) *Optical Optimization*: It includes structure, imaging, light source, and optical path. Structure optimization requires reducing the wiring and sharing structure. The development of vision-tactile simulation [116], [117], [118] offers prior validation for the optimization of imaging, light source, and optical path. It facilitates the dynamic simulation and parameter update.
- 7) *Production Line*: This is the test of the practical application of VBTs. For example, roller-type VBTs are designed for cloth production, increasing the detection efficiency of cloth defects [119]. In [120], a VBT was used to detect surface damage to fruit, improving the quality of fruit picking.
- 8) *Tamper Resistance*: VBTs mainly interfere with outside light. The superposition of ambient light and reflected light affects the display of contact surface deformation. The optical properties of silicone increase the difficulty in designing shading components. Therefore, improving tamper resistance will be a prerequisite for high-precision measurement.

### B. Innovative Hardware Technology

The VBT advances with the times by absorbing interdisciplinary technologies. We think that the following works can seek breakthroughs from the tactile mechanism, ultramicrocameras, and visual presentation of touch. Hence, this article concludes with three directions of cutting-edge technologies:

- 1) *Tactile Bionic Technology*: Tactip [111] adopted the pin structure inspired by the receptor under human skin. In [106], ridges were used on elastic rubber skin to simulate fingerprint perception. In future works, VBTs need to explore more sensitive tactile mechanisms, such as the tactile feedback system of animal tentacles [121] and the tactile system based on compound eye structure [122].
- 2) *Ultramicrocamera Technology*: High performance and ultramicrosize are the development tendencies of modular cameras. The latest research has realized ultramicrocameras with salt grain sizes [123]. It adopted a neural nano-optics imager and a neural feature-based image reconstruction algorithm to decrease image blur distortion. In addition, bionic technology also promoted the improvement of camera technology. Lu et al. [124] reported a multiscale hybrid bionic imaging system

based on fisheye and compound eyes to improve the FOV and resolution. Zhang et al. [125] reported an ultrathin array of microcameras inspired by high contrast and superresolution imaging of insect eyes.

- 3) *Innovative Material*: We hope to improve sensing mechanisms to acquire highly sensitive tactile feedback by combining innovative materials. There are currently some significant works on tactile materials. Liu et al. [126] reported the preparation of an ionic polyacrylamide (PAAm) organogel with properties of tactile perception and interactive color changing. In [127], mechanoluminescence materials (MLs) had luminescence properties under friction, tension, fracture, and compression. Color change and luminescence effect were visual representations of touch. These materials may provide inspiration and a reference for vision-tactile sensing [128].

### VIII. CONCLUSION

This article reviews the hardware technologies of VBTs in the past five years. We discuss each module from the function, material selection, and preparation processes. The perception form and thickness of functional layers are the primary consideration in the contact module. To maintain sensitivity, the hardness of the contact body should adapt to stiffness. Accordingly, the adjustable silicone can provide dynamic adjustment of physical properties. Inside VBTs, the limited lighting conditions require a more elaborate optical design. Via TIR, side illumination solves the problem of uneven light. This mode will play a vital role in the micro-VBTs. Considering reflective characteristics, the match of color light and brightness can maximize the performance of the reflective layer. In addition, the fine and uniform coating ensures imaging quality. Benefiting from the rapid development of microcameras, micro-VBTs can acquire high-performance dynamic tracking and real-time detection. Meanwhile, the microscale size promotes compact structure design, and adjustable lenses provide imaging diversity. In future works, the combination of multitype cameras and functional layers will boost multimodal development.

Based on the discussion of the strengths and weaknesses of existing hardware technologies, we conclude with eight primary issues and challenges. Both performance upgrades and size optimization are inseparable from the support of hardware technologies. Previous literature paid more attention to the structural design and sensing algorithm. We hope to deepen our understanding of hardware through this review. In addition, multidisciplinary and cutting-edge hardware technologies will be a strong driving force for VBT development.

### REFERENCES

- [1] H. Yousef, M. Boukallel, and K. Althoefer, "Tactile sensing for dexterous in-hand manipulation in robotics—A review," *Sens. Actuators A, Phys.*, vol. 167, no. 2, pp. 171–187, Jun. 2011.
- [2] Z. Kappasov, J.-A. Corrales, and V. Perdureau, "Tactile sensing in dexterous robot hands," *Robot. Auto. Syst.*, vol. 74, pp. 195–220, Dec. 2015.
- [3] V. Biazzi-Neto, C. A. F. Marques, A. Frizera-Neto, and A. G. Leal-Junior, "FBG-embedded robotic manipulator tool for structural integrity monitoring from critical strain-stress pair estimation," *IEEE Sensors J.*, vol. 22, no. 6, pp. 5695–5702, Feb. 2022.

- [4] Z. Wang, R. Singh, C. Marques, R. Jha, B. Zhang, and S. Kumar, "Taper-in-taper fiber structure-based LSPR sensor for alanine amino-transferase detection," *Opt. Exp.*, vol. 29, no. 26, pp. 43793–43810, Dec. 2021.
- [5] M. K. Johnson and E. H. Adelson, "Retrographic sensing for the measurement of surface texture and shape," in *Proc. IEEE Conf. Comput. Vis. Pattern Recognit.*, Miami, FL, USA, Jun. 2009, pp. 1070–1077.
- [6] E. Donlon, S. Dong, M. Liu, J. Li, E. Adelson, and A. Rodriguez, "GelSlim: A high-resolution, compact, robust, and calibrated tactile-sensing finger," in *Proc. Int. Conf. Intell. Robots Syst.*, Madrid, Spain, Oct. 2018, pp. 1927–1934.
- [7] C. Chorley, C. Melhuish, T. Pipe, and J. Rossiter, "Development of a tactile sensor based on biologically inspired edge encoding," in *Proc. IEEE Int. Conf. Adv. Robot. (ICAR)*, Munich, Germany, Jun. 2009, pp. 1–6.
- [8] B. Fang et al., "A dual-modal vision-based tactile sensor for robotic hand grasping," in *Proc. IEEE Int. Conf. Robot. Autom. (ICRA)*, Brisbane, QLD, Australia, May 2018, pp. 4740–4745.
- [9] B. Fang, H. Xue, F. Sun, Y. Yang, and R. Zhu, "A cross-modal tactile sensor design for measuring robotic grasping forces," *Ind. Robot. Int. J. Robot. Res. Appl.*, vol. 46, no. 3, pp. 337–344, May 2019.
- [10] F. Sun, B. Fang, H. Xue, H. Liu, and H. Huang, "A novel multi-modal tactile sensor design using thermochromic material," *Sci. China Inf. Sci.*, vol. 62, no. 11, pp. 1–3, Nov. 2019.
- [11] S. Zhang, J. Shan, B. Fang, F. Sun, and H. Liu, "Vision-based tactile perception for soft robotic hand," in *Proc. IEEE Int. Conf. Robot. Biomimetics (ROBIO)*, Dali, China, Dec. 2019, pp. 621–628.
- [12] S. Zhang, J. Shan, B. Fang, and F. Sun, "Soft robotic finger embedded with visual sensor for bending perception," *Robotica*, vol. 39, no. 3, pp. 378–390, Mar. 2021.
- [13] B. Fang et al., "A novel humanoid soft hand with variable stiffness and multi-modal perception," in *Proc. 6th IEEE Int. Conf. Adv. Robot. Mechatronics (ICARM)*, Chongqing, China, Jul. 2021, pp. 99–105.
- [14] B. Fang, X. Long, F. Sun, H. Liu, S. Zhang, and C. Fang, "Tactile-based fabric defect detection using convolutional neural network with attention mechanism," *IEEE Trans. Instrum. Meas.*, vol. 71, pp. 1–9, 2022.
- [15] S. Zhang, J. Shan, F. Sun, B. Fang, and Y. Yang, "Multimode fusion perception for transparent glass recognition," *Ind. Robot. Int. J. Robot. Res. Appl.*, vol. 49, no. 4, pp. 625–633, Jun. 2022.
- [16] M. Bauza, E. Valls, B. Lim, T. Sechopoulos, and A. Rodriguez, "Tactile object pose estimation from the first touch with geometric contact rendering," 2020, *arXiv:2012.05205*.
- [17] R. Li et al., "Localization and manipulation of small parts using GelSight tactile sensing," in *Proc. IEEE/RSJ Int. Conf. Intell. Robots Syst.*, Chicago, IL, USA, Sep. 2014, pp. 3988–3993.
- [18] S. Wang et al., "3D shape perception from monocular vision, touch, and shape priors," in *Proc. IEEE/RSJ Int. Conf. Intell. Robots Syst. (IROS)*, Madrid, Spain, Oct. 2018, pp. 1606–1613.
- [19] S. Dong, W. Yuan, and E. H. Adelson, "Improved GelSight tactile sensor for measuring geometry and slip," in *Proc. IEEE Int. Conf. Intell. Robots Syst.*, Vancouver, BC, Canada, Sep. 2017, pp. 137–144.
- [20] S. Luo, W. Yuan, E. Adelson, A. G. Cohn, and R. Fuentes, "ViTac: Feature sharing between vision and tactile sensing for cloth texture recognition," in *Proc. IEEE Int. Conf. Robot. Automat. (ICRA)*, Brisbane, QLD, Australia, May 2018, pp. 2722–2727.
- [21] B. Ward-Cherrier, N. Pestell, and N. F. Lepora, "NeuroTac: A neuromorphic optical tactile sensor applied to texture recognition," in *Proc. IEEE Int. Conf. Robot. Autom. (ICRA)*, Paris, France, May 2020, pp. 2654–2660.
- [22] C. Sferrazza, A. Wahlsten, C. Trueeb, and R. D'Andrea, "Ground truth force distribution for learning-based tactile sensing: A finite element approach," *IEEE Access*, vol. 7, pp. 173438–173449, 2019.
- [23] R. Wang, C. Jiang, B. Yang, and J. Liu, "A novel vision-based tactile sensor using particle image velocimetry for multi-modal object detection and force sensing," in *Proc. IEEE 34th Int. Conf. Micro Electro Mech. Syst. (MEMS)*, Gainesville, FL, USA, Jan. 2021, pp. 764–767.
- [24] W. Li, A. Alomainy, I. Vitanov, Y. Noh, P. Qi, and K. Althoefer, "F-TOUCH sensor: Concurrent geometry perception and multi-axis force measurement," *IEEE Sensors J.*, vol. 21, no. 4, pp. 4300–4309, Feb. 2021.
- [25] T. Zhang, Y. Cong, X. Li, and Y. Peng, "Robot tactile sensing: Vision based tactile sensor for force perception," in *Proc. IEEE 8th Annu. Int. Conf. Technol. Autom., Control, Intell. Syst. (CYBER)*, Tianjin, China, Jul. 2018, pp. 1360–1365.
- [26] J. Li, S. Dong, and E. Adelson, "Slip detection with combined tactile and visual information," in *Proc. IEEE Int. Conf. Robot. Autom. (ICRA)*, Brisbane, QLD, Australia, May 2018, pp. 7772–7777.
- [27] F. Baghaei Naeini, D. Makris, D. Gan, and Y. Zweiri, "Dynamic-vision-based force measurements using convolutional recurrent neural networks," *Sensors*, vol. 20, no. 16, p. 4469, Aug. 2020.
- [28] W. Yuan, C. Zhu, A. Owens, M. A. Srinivasan, and E. H. Adelson, "Shape-independent hardness estimation using deep learning and a GelSight tactile sensor," in *Proc. IEEE Int. Conf. Robot. Autom. (ICRA)*, Singapore, Jun. 2017, pp. 951–958.
- [29] W. Yuan, Y. Mo, S. Wang, and E. H. Adelson, "Active clothing material perception using tactile sensing and deep learning," in *Proc. IEEE Int. Conf. Robot. Autom. (ICRA)*, Brisbane, QLD, Australia, May 2018, pp. 4842–4849.
- [30] W. Yuan, S. Wang, S. Dong, and E. Adelson, "Connecting look and feel: Associating the visual and tactile properties of physical materials," in *Proc. IEEE Conf. Comput. Vis. Pattern Recognit.*, Honolulu, HI, USA, Jun. 2017, pp. 5580–5588.
- [31] J. Li, S. Dong, and E. H. Adelson, "End-to-end pixelwise surface normal estimation with convolutional neural networks and shape reconstruction using GelSight sensor," in *Proc. IEEE Int. Conf. Robot. Biomimetics (ROBIO)*, Kuala Lumpur, Malaysia, Dec. 2018, pp. 1292–1297.
- [32] J. Jiang, G. Cao, D. F. Gomes, and S. Luo, "Vision-guided active tactile perception for crack detection and reconstruction," in *Proc. 29th Medit. Conf. Control Autom. (MED)*, Bari, Italy, Jun. 2021, pp. 930–936.
- [33] H. Song, T. Bhattacharjee, and S. S. Srinivasa, "Sensing shear forces during food manipulation: Resolving the trade-off between range and sensitivity," in *Proc. Int. Conf. Robot. Autom. (ICRA)*, Montreal, QC, Canada, May 2019, pp. 8367–8373.
- [34] S. Dong and A. Rodriguez, "Tactile-based insertion for dense box-packing," in *Proc. IEEE/RSJ Int. Conf. Intell. Robots Syst. (IROS)*, Macao, China, Nov. 2019, pp. 7953–7960.
- [35] J. Lin, R. Calandra, and S. Levine, "Learning to identify object instances by touch: Tactile recognition via multimodal matching," in *Proc. Int. Conf. Robot. Autom. (ICRA)*, Montreal, QC, Canada, May 2019, pp. 3644–3650.
- [36] R. Calandra et al., "More than a feeling: Learning to grasp and regrasp using vision and touch," *IEEE Robot. Autom. Lett.*, vol. 3, no. 4, pp. 3300–3307, Oct. 2018.
- [37] J. W. James, A. Church, L. Cramphorn, and N. F. Lepora, "Tactile model O: Fabrication and testing of a 3D-printed, three-fingered tactile robot hand," *Soft Robot.*, vol. 8, no. 5, pp. 594–610, Oct. 2021.
- [38] T. Anzai and K. Takahashi, "Deep gated multi-modal learning: In-hand object pose changes estimation using tactile and image data," in *Proc. IEEE/RSJ Int. Conf. Intell. Robots Syst. (IROS)*, Las Vegas, NV, USA, Oct. 2020, pp. 9361–9368.
- [39] F. R. Hogan, M. Bauza, O. Canal, E. Donlon, and A. Rodriguez, "Tactile regrasp: Grasp adjustments via simulated tactile transformations," in *Proc. IEEE/RSJ Int. Conf. Intell. Robots Syst. (IROS)*, Madrid, Spain, Oct. 2018, pp. 2963–2970.
- [40] Y. She, S. Wang, S. Dong, N. Sunil, A. Rodriguez, and E. Adelson, "Cable manipulation with a tactile-reactive gripper," *Int. J. Robot. Res.*, vol. 40, nos. 12–14, pp. 1385–1401, Aug. 2021.
- [41] S. Cui, R. Wang, J. Hu, J. Wei, S. Wang, and Z. Lou, "In-hand object localization using a novel high-resolution visuotactile sensor," *IEEE Trans. Ind. Electron.*, vol. 69, no. 6, pp. 6015–6025, Jun. 2021.
- [42] C. Wang, S. Wang, B. Romero, F. Veiga, and E. Adelson, "SwingBot: Learning physical features from in-hand tactile exploration for dynamic swing-up manipulation," in *Proc. IEEE/RSJ Int. Conf. Intell. Robots Syst. (IROS)*, Las Vegas, NV, USA, Oct. 2020, pp. 5633–5640.
- [43] A. Yamaguchi and C. G. Atkeson, "Recent progress in tactile sensing and sensors for robotic manipulation: Can we turn tactile sensing into vision?" *Adv. Robot.*, vol. 33, no. 14, pp. 661–673, Jun. 2019.
- [44] U. H. Shah, R. Muthusamy, D. Gan, Y. Zweiri, and L. Seneviratne, "On the design and development of vision-based tactile sensors," *J. Intell. Robot. Syst.*, vol. 102, no. 4, pp. 1–27, Jul. 2021.
- [45] K. Shimomura, "Tactile image sensors employing camera: A review," *Sensors*, vol. 19, no. 18, p. 3933, 2019.
- [46] N. F. Lepora and J. Lloyd, "Optimal deep learning for robot touch: Training accurate pose models of 3D surfaces and edges," *IEEE Robot. Autom. Mag.*, vol. 27, no. 2, pp. 66–77, Jun. 2020.
- [47] W. Chen, H. Khamis, I. Birnieks, N. F. Lepora, and S. J. Redmond, "Tactile sensors for friction estimation and incipient slip detection—Toward dexterous robotic manipulation: A review," *IEEE Sensors J.*, vol. 18, no. 22, pp. 9049–9064, Nov. 2018.



- [48] W. Yuan, S. Dong, and E. H. Adelson, "GelSight: High-resolution robot tactile sensors for estimating geometry and force," *Sensors*, vol. 17, no. 12, p. 2762, 2017.
- [49] A. C. Abad and A. Ranasinghe, "Visuotactile sensors with emphasis on GelSight sensor: A review," *IEEE Sensors J.*, vol. 20, no. 14, pp. 7628–7638, Jul. 2020.
- [50] B. Ward-Cherrier et al., "The TacTip family: Soft optical tactile sensors with 3D-printed biomimetic morphologies," *Soft Robot.*, vol. 5, no. 2, pp. 216–227, Apr. 2018.
- [51] N. F. Lepora, "Soft biomimetic optical tactile sensing with the TacTip: A review," *IEEE Sensors J.*, vol. 21, no. 19, pp. 21131–21143, Oct. 2021.
- [52] M. Bauza, O. Canal, and A. Rodriguez, "Tactile mapping and localization from high-resolution tactile imprints," in *Proc. Int. Conf. Robot. Autom. (ICRA)*, Montreal, QC, Canada, May 2019, pp. 3811–3817.
- [53] W. Yuan, R. Li, M. A. Srinivasan, and E. H. Adelson, "Measurement of shear and slip with a GelSight tactile sensor," in *Proc. IEEE Int. Conf. Robot. Automat.*, Seattle, WA, USA, May 2015, pp. 304–311.
- [54] R. Sui, L. Zhang, T. Li, and Y. Jiang, "Incipient slip detection method with vision-based tactile sensor based on distribution force and deformation," *IEEE Sensors J.*, vol. 21, no. 22, pp. 25973–25985, Nov. 2021.
- [55] S. Dong, D. Ma, E. Donlon, and A. Rodriguez, "Maintaining grasps within slipping bounds by monitoring incipient slip," in *Proc. Int. Conf. Robot. Autom. (ICRA)*, Montreal, QC, Canada, May 2019, pp. 3818–3824.
- [56] R. Kolamuri, Z. Si, Y. Zhang, A. Agarwal, and W. Yuan, "Improving grasp stability with rotation measurement from tactile sensing," in *Proc. IEEE/RSJ Int. Conf. Intell. Robots Syst. (IROS)*, Prague, Czech Republic, Sep. 2021, pp. 6809–6816.
- [57] N. Kuppuswamy, A. Castro, C. Phillips-Grafflin, A. Alspach, and R. Tedrake, "Fast model-based contact patch and pose estimation for highly deformable dense-geometry tactile sensors," *IEEE Robot. Autom. Lett.*, vol. 5, no. 2, pp. 1811–1818, Apr. 2021.
- [58] A. Alspach, K. Hashimoto, N. Kuppuswamy, and R. Tedrake, "Soft-bubble: A highly compliant dense geometry tactile sensor for robot manipulation," in *Proc. 2nd IEEE Int. Conf. Soft Robot. (RoboSoft)*, Seoul, South Korea, Apr. 2019, pp. 597–604.
- [59] R. Ambrus, V. Guizilini, N. Kuppuswamy, A. Beaulieu, A. Gaidon, and A. Alspach, "Monocular depth estimation for soft visuotactile sensors," in *Proc. IEEE 4th Int. Conf. Soft Robot. (RoboSoft)*, New Haven, CT, USA, Apr. 2021, pp. 643–649.
- [60] S. Li, L. Ye, C. Xia, X. Wang, and B. Liang, "Design of a tactile sensing robotic gripper and its grasping method," in *Proc. IEEE Int. Conf. Syst., Man, Cybern. (SMC)*, Melbourne, QLD, Australia, Oct. 2021, pp. 894–901.
- [61] Y. She, S. Q. Liu, P. Yu, and E. Adelson, "Exoskeleton-covered soft finger with vision-based proprioception and tactile sensing," in *Proc. IEEE Int. Conf. Robot. Autom. (ICRA)*, Paris, France, May 2020, pp. 10075–10081.
- [62] D. F. Gomes, Z. Lin, and S. Luo, "GelTip: A finger-shaped optical tactile sensor for robotic manipulation," in *Proc. IEEE/RSJ Int. Conf. Intell. Robots Syst. (IROS)*, Las Vegas, NV, USA, Oct. 2020, pp. 9903–9909.
- [63] A. Yamaguchi and C. G. Atkeson, "Tactile behaviors with the vision-based tactile sensor FingerVision," *Int. J. Humanoid Robot.*, vol. 16, no. 3, Jul. 2019, Art. no. 1940002.
- [64] D. Ma, E. Donlon, S. Dong, and A. Rodriguez, "Dense tactile force estimation using GelSlim and inverse FEM," in *Proc. IEEE Int. Conf. Robot. Automat. (ICRA)*, Montreal, QC, Canada, May 2019, pp. 5418–5424.
- [65] Y. Du, G. Zhang, Y. Zhang, and M. Y. Wang, "High-resolution 3-dimensional contact deformation tracking for FingerVision sensor with dense random color pattern," *IEEE Robot. Autom. Lett.*, vol. 6, no. 2, pp. 2147–2154, Apr. 2021.
- [66] C. Sferrazza and R. D'Andrea, "Design, motivation and evaluation of a full-resolution optical tactile sensor," *Sensors*, vol. 19, no. 4, p. 928, Feb. 2019.
- [67] G. Soter, M. Garrad, A. T. Conn, H. Hauser, and J. Rossiter, "Skinflow: A soft robotic skin based on fluidic transmission," in *Proc. 2nd IEEE Int. Conf. Soft Robot. (RoboSoft)*, Seoul, South Korea, Apr. 2019, pp. 355–360.
- [68] Z. Kappasov, D. Baimukashev, Z. Kuanyshuly, Y. Massalin, A. Urazbayev, and H. A. Varol, "Color-coded fiber-optic tactile sensor for an elastomeric robot skin," in *Proc. Int. Conf. Robot. Autom. (ICRA)*, Montreal, QC, Canada, May 2019, pp. 2146–2152.
- [69] C. Yu, L. Lindenroth, J. Hu, J. Back, G. Abrahams, and H. Liu, "A vision-based soft somatosensory system for distributed pressure and temperature sensing," *IEEE Robot. Autom. Lett.*, vol. 5, no. 2, pp. 3323–3329, Apr. 2020.
- [70] B. W. McInroe, C. L. Chen, K. Y. Goldberg, R. Bajcsy, and R. S. Fearing, "Towards a soft fingertip with integrated sensing and actuation," in *Proc. IEEE/RSJ Int. Conf. Intell. Robots Syst. (IROS)*, Madrid, Spain, Oct. 2018, pp. 6437–6444.
- [71] I. Huang and R. Bajcsy, "High resolution soft tactile interface for physical human-robot interaction," in *Proc. IEEE Int. Conf. Robot. Autom. (ICRA)*, Paris, France, May 2020, pp. 1705–1711.
- [72] M. Polic, I. Krajacic, N. Lepora, and M. Orsag, "Convolutional autoencoder for feature extraction in tactile sensing," *IEEE Robot. Autom. Lett.*, vol. 4, no. 4, pp. 3671–3678, Oct. 2020.
- [73] G. Soter, A. Conn, H. Hauser, N. F. Lepora, and J. Rossiter, "MultiTip: A multimodal mechano-thermal soft fingertip," in *Proc. IEEE Int. Conf. Soft Robot. (RoboSoft)*, Apr. 2018, pp. 239–244.
- [74] B. Romero, F. Veiga, and E. Adelson, "Soft, round, high resolution tactile fingertip sensors for dexterous robotic manipulation," in *Proc. IEEE Int. Conf. Robot. Autom. (ICRA)*, Paris, France, May 2020, pp. 4796–4802.
- [75] I. Taylor, S. Dong, and A. Rodriguez, "GelSlim3.0: High-resolution measurement of shape, force and slip in a compact tactile-sensing finger," 2021, *arXiv:2103.12269*.
- [76] A. Wilson, S. Wang, B. Romero, and E. Adelson, "Design of a fully actuated robotic hand with multiple Gelsight tactile sensors," in *Proc. IEEE Int. Conf. Robot. Autom. (ICRA)*, Philadelphia, PA, USA, May 2022, pp. 10781–10787.
- [77] L. Van Duong, R. Asahina, J. Wang, and V. A. Ho, "Development of a vision-based soft tactile muscularis," in *Proc. 2nd IEEE Int. Conf. Soft Robot. (RoboSoft)*, Seoul, South Korea, Apr. 2019, pp. 343–348.
- [78] T. Sakuma, F. Von Drigalski, M. Ding, J. Takamatsu, and T. Ogasawara, "A universal gripper using optical sensing to acquire tactile information and membrane deformation," in *Proc. IEEE/RSJ Int. Conf. Intell. Robots Syst. (IROS)*, Madrid, Spain, Oct. 2018, pp. 1–9.
- [79] T. Sakuma, E. Phillips, G. A. G. Ricardez, M. Ding, J. Takamatsu, and T. Ogasawara, "A parallel gripper with a universal fingertip device using optical sensing and jamming transition for maintaining stable grasps," in *Proc. IEEE/RSJ Int. Conf. Intell. Robots Syst. (IROS)*, Macau, China, Nov. 2019, pp. 5814–5819.
- [80] N. Pestell, J. Lloyd, J. Rossiter, and N. F. Lepora, "Dual-modal tactile perception and exploration," *IEEE Robot. Autom. Lett.*, vol. 3, no. 2, pp. 1033–1040, Apr. 2018.
- [81] N. Pestell, L. Cramphorn, F. Papadopoulos, and N. F. Lepora, "A sense of touch for the shadow modular grasper," *IEEE Robot. Autom. Lett.*, vol. 4, no. 2, pp. 2220–2226, Apr. 2019.
- [82] C. Xiang, J. Guo, and J. Rossiter, "Soft-smart robotic end effectors with sensing, actuation, and gripping capabilities," *Smart Mater. Struct.*, vol. 28, no. 5, Apr. 2019, Art. no. 055034.
- [83] A. C. Abad and A. Ranasinghe, "Low-cost GelSight with UV markings: Feature extraction of objects using AlexNet and optical flow without 3D image reconstruction," in *Proc. IEEE Int. Conf. Robot. Autom. (ICRA)*, Paris, France, May 2020, pp. 3680–3685.
- [84] X. Lin and M. Wiertelowski, "Sensing the frictional state of a robotic skin via subtractive color mixing," *IEEE Robot. Autom. Lett.*, vol. 4, no. 3, pp. 2386–2392, Jul. 2019.
- [85] R. Ouyang and R. Howe, "Low-cost fiducial-based 6-Axis force-torque sensor," in *Proc. IEEE Int. Conf. Robot. Autom. (ICRA)*, Paris, France, May 2020, pp. 1653–1659.
- [86] X. Lin, L. Willemet, A. Bailleul, and M. Wiertelowski, "Curvature sensing with a spherical tactile sensor using the color-interference of a marker array," in *Proc. IEEE Int. Conf. Robot. Autom. (ICRA)*, Paris, France, May 2020, pp. 603–609.
- [87] G. Zhang, Y. Du, Y. Zhang, and M. Y. Wang, "A tactile sensing foot for single robot leg stabilization," in *Proc. IEEE Int. Conf. Robot. Autom. (ICRA)*, Xi'an, China, May 2021, pp. 14076–14082.
- [88] N. Kuppuswamy, A. Alspach, A. Uttamchandani, S. Creasey, T. Ikeda, and R. Tedrake, "Soft-bubble grippers for robust and perceptive manipulation," in *Proc. IEEE/RSJ Int. Conf. Intell. Robots Syst. (IROS)*, Las Vegas, NV, USA, Oct. 2020, pp. 9917–9924.
- [89] Y. Yang, X. Wang, Z. Zhou, J. Zeng, and H. Liu, "An enhanced FingerVision for contact spatial surface sensing," *IEEE Sensors J.*, vol. 21, no. 15, pp. 16492–16502, Aug. 2021.
- [90] E. A. Stone, N. F. Lepora, and D. A. W. Barton, "Walking on TacTip toes: A tactile sensing foot for walking robots," in *Proc. IEEE/RSJ Int. Conf. Intell. Robots Syst. (IROS)*, Las Vegas, NV, USA, Jan. 2021, pp. 9869–9875.

- [91] A. Padmanabha, F. Ebert, S. Tian, R. Calandra, C. Finn, and S. Levine, "OmniTact: A multi-directional high-resolution touch sensor," in *Proc. IEEE Int. Conf. Robot. Autom. (ICRA)*, Paris, France, May 2020, pp. 618–624.
- [92] S. Wang, Y. She, B. Romero, and E. Adelson, "GelSight wedge: Measuring high-resolution 3D contact geometry with a compact robot finger," in *Proc. IEEE Int. Conf. Robot. Autom. (ICRA)*, Xi'an, China, May 2021, pp. 6468–6475.
- [93] D. F. Gomes, Z. Lin, and S. Luo, "Blocks world of touch: Exploiting the advantages of all-around finger sensing in robot grasping," *Frontiers Robot. AI*, vol. 7, Nov. 2020, Art. no. 541661.
- [94] A. C. Abad, D. Reid, and A. Ranasinghe, "HaptiTemp: A next-generation thermosensitive GelSight-like visuotactile sensor," *IEEE Sensors J.*, vol. 22, no. 3, pp. 2722–2734, Feb. 2022.
- [95] D. Baimukashev, Z. Kappasov, and H. A. Varol, "Shear, torsion and pressure tactile sensor via plastic optofiber guided imaging," *IEEE Robot. Autom. Lett.*, vol. 5, no. 2, pp. 2618–2625, Apr. 2020.
- [96] H. Jiang, Y. Yan, X. Zhu, and C. Zhang, "A 3-D surface reconstruction with shadow processing for optical tactile sensors," *Sensors*, vol. 18, no. 9, p. 2785, Aug. 2018.
- [97] M. Lambeta et al., "DIGIT: A novel design for a low-cost compact high-resolution tactile sensor with application to in-hand manipulation," *IEEE Robot. Autom. Lett.*, vol. 5, no. 3, pp. 3838–3845, Jul. 2020.
- [98] Y. Zhang, Z. Kan, Y. Yang, Y. A. Tse, and M. Y. Wang, "Effective estimation of contact force and torque for vision-based tactile sensors with Helmholtz–Hodge decomposition," *IEEE Robot. Autom. Lett.*, vol. 4, no. 4, pp. 4094–4101, Oct. 2019.
- [99] P. Werner, M. Hofer, C. Sferazza, and R. D'Andrea, "Vision-based proprioceptive sensing: Tip position estimation for a soft inflatable bellow actuator," in *Proc. IEEE/RSJ Int. Conf. Intell. Robots Syst. (IROS)*, Las Vegas, NV, USA, Oct. 2020, pp. 8889–8896.
- [100] A. J. Fernandez, H. Weng, P. B. Umbanhowar, and K. M. Lynch, "Visi-flex: A low-cost compliant tactile fingertip for force, torque, and contact sensing," *IEEE Robot. Autom. Lett.*, vol. 6, no. 2, pp. 3009–3016, Apr. 2021.
- [101] F. R. Hogan, M. Jenkin, S. Rezaei-Shoshtari, Y. Girdhar, D. Meger, and G. Dudek, "Seeing through your skin: Recognizing objects with a novel visuotactile sensor," in *Proc. IEEE Winter Conf. Appl. Comput. Vis. (WACV)*, Waikoloa, HI, USA, Jan. 2021, pp. 1217–1226.
- [102] H. Sun, K. J. Kuchenbecker, and G. Martius, "A soft thumb-sized vision-based sensor with accurate all-round force perception," *Nature Mach. Intell.*, vol. 4, no. 2, pp. 135–145, Feb. 2022.
- [103] R. Patel, R. Ouyang, B. Romero, and E. Adelson, "Digger finger: GelSight tactile sensor for object identification inside granular media," 2021, *arXiv:2102.10230*.
- [104] C. Trueeb, C. Sferazza, and R. D'Andrea, "Towards vision-based robotic skins: A data-driven, multi-camera tactile sensor," in *Proc. 3rd IEEE Int. Conf. Soft Robot. (RoboSoft)*, New Haven, CT, USA, May 2020, pp. 333–338.
- [105] L. Zhang, Y. Wang, and Y. Jiang, "Tac3D: A novel vision-based tactile sensor for measuring forces distribution and estimating friction coefficient distribution," 2022, *arXiv:2202.06211*.
- [106] J. W. James, S. J. Redmond, and N. F. Lepora, "A biomimetic tactile fingerprint induces incipient slip," in *Proc. IEEE/RSJ Int. Conf. Intell. Robots Syst. (IROS)*, Las Vegas, NV, USA, Oct. 2020, pp. 9833–9839.
- [107] Z. Xu, Y. Zheng, and S. A. Rawashdeh, "A simple robotic fingertip sensor using imaging and shallow neural networks," *IEEE Sensors J.*, vol. 19, no. 19, pp. 8878–8886, Oct. 2019.
- [108] N. F. Lepora et al., "Towards integrated tactile sensorimotor control in anthropomorphic soft robotic hands," in *Proc. IEEE Int. Conf. Robot. Autom. (ICRA)*, Xi'an, China, May 2021, pp. 1622–1628.
- [109] L. Van Duong and V. A. Ho, "Large-scale vision-based tactile sensing for robot links: Design, modeling, and evaluation," *IEEE Trans. Robot.*, vol. 37, no. 2, pp. 390–403, Apr. 2021.
- [110] Y. Zhang, Z. Kan, Y. A. Tse, Y. Yang, and M. Y. Wang, "FingerVision tactile sensor design and slip detection using convolutional LSTM network," 2018, *arXiv:1810.02653*.
- [111] N. Pestell, T. Griffith, and N. F. Lepora, "Artificial SA-I and RA-I afferents for tactile sensing of ridges and gratings," *J. Roy. Soc. Interface*, vol. 19, no. 189, Apr. 2022, Art. no. 20210822.
- [112] A. Yamaguchi, "Fingervision for tactile behaviors, manipulation, and haptic feedback teleoperation," in *Proc. 4th IEEE Int. Workshop Sens., Actuation, Motion Control, Optim. (SAMCON)*, Tokyo, Japan, Mar. 2016.
- [113] K. Kumagai and K. Shimonomura, "Event-based tactile image sensor for detecting spatio-temporal fast phenomena in contacts," in *Proc. IEEE World Haptics Conf. (WHC)*, Tokyo, Japan, Jul. 2019, pp. 343–348.
- [114] F. B. Naeini et al., "A novel dynamic-vision-based approach for tactile sensing applications," *IEEE Trans. Instrum. Meas.*, vol. 69, pp. 1881–1893, 2022.
- [115] Z. Erickson, E. Xing, B. Srirangam, S. Chernova, and C. C. Kemp, "Multimodal material classification for robots using spectroscopy and high resolution texture imaging," in *Proc. IEEE/RSJ Int. Conf. Intell. Robots Syst. (IROS)*, Las Vegas, NV, USA, Oct. 2020, pp. 10452–10459.
- [116] D. F. Gomes, P. Paoletti, and S. Luo, "Generation of GelSight tactile images for Sim2Real learning," *IEEE Robot. Autom. Lett.*, vol. 6, no. 2, pp. 4177–4184, Apr. 2021.
- [117] A. Agarwal, T. Man, and W. Yuan, "Simulation of vision-based tactile sensors using physics based rendering," in *Proc. IEEE Int. Conf. Robot. Autom. (ICRA)*, Xi'an, China, May 2021, pp. 1–7.
- [118] Z. Si and W. Yuan, "Taxim: An example-based simulation model for GelSight tactile sensors," *IEEE Robot. Autom. Lett.*, vol. 7, no. 2, pp. 2361–2368, Apr. 2022.
- [119] X. Long, B. Fang, Y. Zhang, G. Luo, and F. Sun, "Fabric defect detection using tactile information," in *Proc. IEEE Int. Conf. Robot. Autom. (ICRA)*, Xi'an, China, May 2021, pp. 11169–11174.
- [120] Y. Chen, J. Lin, X. Du, B. Fang, F. Sun, and S. Li, "Non-destructive fruit firmness evaluation using vision-based tactile information," in *Proc. Int. Conf. Robot. Autom. (ICRA)*, Philadelphia, PA, USA, May 2022, pp. 2303–2309.
- [121] N. F. Lepora, M. Pearson, and L. Cramphorn, "TacWhiskers: Biomimetic optical tactile whiskered robots," in *Proc. IEEE/RSJ Int. Conf. Intell. Robots Syst. (IROS)*, Madrid, Spain, Oct. 2018, pp. 7628–7634.
- [122] L. Song, H. Zhu, Y. Zheng, M. Zhao, C. A. T. Tee, and F. Fang, "Bionic compound eye-inspired high spatial and sensitive tactile sensor," *IEEE Trans. Instrum. Meas.*, vol. 70, pp. 1–8, 2021.
- [123] E. Tseng et al., "Neural nano-optics for high-quality thin lens imaging," *Nature Commun.*, vol. 12, no. 1, pp. 1–7, 2021.
- [124] W. Lu, S. Chen, Y. Xiong, and J. Liu, "A single ball lens-based hybrid biomimetic fish eye/compound eye imaging system," *Opt. Commun.*, vol. 480, Feb. 2021, Art. no. 126458.
- [125] Y. Zhang, X. Chen, M. Y. Wang, and H. Yu, "Multidimensional tactile sensor with a thin compound eye-inspired imaging system," *Soft Robot.*, Oct. 2021. [Online]. Available: <https://www.liebertpub.com/doi/full/10.1089/soro.2020.0202>
- [126] Y.-F. Liu et al., "Bioinspired color-changeable organogel tactile sensor with excellent overall performance," *ACS Appl. Mater. Interfaces*, vol. 12, no. 44, pp. 49866–49875, Oct. 2020.
- [127] X. Li et al., "Broadband multimodal emission in Sb-doped CaZnOS-layered semiconductors," *Sci. China Mater.*, vol. 65, no. 5, pp. 1329–1336, May 2022.
- [128] D. Peng et al., "A ZnS/CaZnOS heterojunction for efficient mechanical-to-optical energy conversion by conduction band offset," *Adv. Mater.*, vol. 32, no. 16, Mar. 2020, Art. no. 1907747.
- [129] P. Griffa, C. Sferazza, and R. D'Andrea, "Leveraging distributed contact force measurements for slip detection: A physics-based approach enabled by a data-driven tactile sensor," in *Proc. Int. Conf. Robot. Autom. (ICRA)*, Philadelphia, PA, USA, May 2022, pp. 4826–4832.
- [130] W. Kim, W. D. Kim, J.-J. Kim, C.-H. Kim, and J. Kim, "UVtac: Switchable UV marker-based tactile sensing finger for effective force estimation and object localization," *IEEE Robot. Autom. Lett.*, vol. 7, no. 3, pp. 6036–6043, Jul. 2022.
- [131] J. Jiang, G. Cao, D. F. Gomes, and S. Luo, "Vision-guided active tactile perception for crack detection and reconstruction," in *Proc. 29th Medit. Conf. Control Autom. (MED)*, Puglia, Italy, Jun. 2021, pp. 930–936.
- [132] C. Sferazza and R. D'Andrea, "Transfer learning for vision-based tactile sensing," in *Proc. IEEE/RSJ Int. Conf. Intell. Robots Syst. (IROS)*, Macau, China, Nov. 2019, pp. 7961–7967.